Simulation and Study of the Stokes Vector in a Precipitating Atmosphere

by

Ian Stuart Adams
B.S.E.E. University of Central Florida, 2001
M.S.E.E. University of Central Florida, 2005

A dissertation submitted in partial fulfillment of the requirements
for the degree of Doctor of Philosophy
in the School of Electrical Engineering and Computer Science
in the College of Engineering and Computer Science
at the University of Central Florida
Orlando, Florida

Fall Term
2007

Major Professor: W. Linwood Jones

ABSTRACT

Precipitation is a dominating quantity in microwave radiometry. The large emission and scattering signals of rain and ice, respectively, introduce large contributions to the measured brightness temperature. While this allows for accurate sensing of precipitation, it also results in degraded performance when retrieving other geophysical parameters, such as near-surface ocean winds. In particular, the retrieval of wind direction requires precise knowledge of polarization, and nonspherical particles can result in a change in the polarization of incident radiation. The aim of this dissertation is to investigate the polarizing effects of precipitation in the atmosphere, including the existence of a precipitation signal in the third Stokes parameter, and compare these effects with the current sensitivities of passive wind vector retrieval algorithms. Realistic simulated precipitation profiles give hydrometeor water contents which are input into a vector radiative transfer model. Brightness temperatures are produced within the model using a reverse Monte Carlo method. Results are produced at three frequencies of interest to microwave polarimetry, 10.7 GHz, 18.7 GHz, and 37.0 GHz, for the first 3 components of the Stokes vector.

To my parents, who always pushed me to do my best even when it was painful for all of us, and to my wife Chani and daughter Alia, who inspire me in all that I do.

ACKNOWLEDGMENTS

I would like to thank my advisor and mentor Dr. Linwood Jones for all of the guidance that he has given me over the past 7 years. I would also like my committee members–Dr. Takis Kasparis, Dr. Peter Gaiser, Dr. Thomas Wu, Dr. Larry Andrews, and Mr. Jim Johnson–for all of their time and consideration. I am very grateful to Dr. Peter Gaiser and Dr. Mike Bettenhausen at the Naval Research Lab, Remote Sensing Division, for the opportunity to join their team and for the time to finish this dissertation. Finally, I would like to thank Dr. Chris Kummerow and Jody Crook at Colorado State University for giving me access to their radiative transfer code and to the Goddard Cumulus Ensemble data.

TABLE OF CONTENTS

LIST OF FIGURES

LIST OF TABLES

CHAPTER 1
INTRODUCTION

The advent of microwave radiometry has revolutionized the ability to remotely sense meteorologic quantities over land and especially ocean. Instruments such as the Special Sensor Microwave Imager (SSM/I) provide the basis for retrieving quantities such as water vapor, sea surface temperature, ocean surface wind speed, and precipitation [1]. Due to the complexities of tropospheric cloud structures, the retrieval of precipitation is particularly difficult. The large microwave signal of rain also interferes with the measurement of other oceanic quantities. To improve the understanding of precipitation, the Tropical Rain Measuring Mission (TRMM) was launched in 1997. In addition to a microwave radiometer, TRMM carries a profiling radar to retrieve precipitation characteristics. The profiling properties of the radar are used to investigate the vertical structure of precipitation while the radiometer can discern liquid and ice quantities using a multifrequency retrieval algorithm [2], [3].

Recently, the WindSat Polarimetric Radiometer was developed and launched to utilize fully polarimetric measurements in retrieving atmospheric, oceanographic, and geophysical parameters [4]. While previous instruments made use of horizontally and vertically polarized brightness temperatures, WindSat measures the entire Stokes vector. WindSat is, thus, the first spaceborne passive instrument capable of measuring

wind direction, a quantity previously only measured using radar; however, like previous multifrequency radiometers, it is also capable of measuring water vapor, cloud, and precipitation. While the third and fourth Stokes parameters, which are used in wind direction retrievals, are insensitive to most atmospheric parameters, precipitation adversely affects the ability to obtain accurate ocean surface measurements [5].

The purpose of this dissertation is to study the polarization of microwave radiation in a precipitating atmosphere. By simulating the transfer of microwave radiation through a vertically inhomogeneous cloud structure, microwave radiances are generated for a variety of instrument configurations under various precipitating conditions. The shapes of rain and ice hydrometeors are modeled so as to simulate the effect of particle shape on polarization. The remainder of this chapter briefly outlines the WindSat sensor with respect to the broader picture of microwave radiometry as well as useful quantities derived from Maxwell's equations. Chapter 2 details how electromagnetic radiation interacts with individual particles and groups of particles and Chapter 3 gives a more in-depth explanation of the significance of these electromagnetic properties. Chapter 4 lists the components of the radiative transfer model used for the simulations. Chapter 5 explains the simulations that were conducted for this study and Chapter 6 details simulation results.

1.1 Microwave Radiometry: The WindSat Example

WindSat is a multifrequency, fully-polarized microwave radiometer, launched aboard the Coriolis satellite on January 6, 2003. The instrument utilizes five frequency channels: 6.8 GHz, 10.7 GHz, 18.7 GHz, 23.8 GHz, and 37.0 GHz. The 10.7-, 18.7-, and 37.0-GHz channels are fully-polarized, i.e., capable of measuring the full Stokes vector, while the 6.8- and 23.8-GHz channels only measure horizontal and vertical radiances. The 6.8-GHz and 10.7-GHz horizontal and vertical radiances allow for retrieval of sea surface temperature due to the higher sensitivity in lower frequencies to this quantity [6]. The 18.7-GHz and 23.8-GHz horizontal and vertical measurements are used to retrieve integrated water vapor, as there is an absorption line at 22.235 GHz [3], [7]. Wind vector (speed and direction) retrievals require all brightness temperature channels, while only the horizontal and vertical radiance (only vertical at 23.8 GHz) apply to precipitation retrievals.

Since the emission and scattering properties of precipitation are quite strong, precipitation presents a large amount of interference when trying to obtain other environmental information. Of particular interest are the polarizing effects of rain, especially that of the third Stokes parameters. This dissertation documents the simulation of the fully-polarized radiances at 10.7, 18.7 and 37.0 GHz with the purpose of determining what type of interference may be present in radiometric measurements. A Lambertian

(non-directional and non-polarized) surface describes the surface boundary to isolate the polarizing effects of precipitation.

1.2 Wave Propagation and Polarization

Understanding how electromagnetic radiation interacts with precipitation requires knowledge of the phenomena behind the propagation and the state of the radiation– the intensity and polarization. This section outlines the plane wave form of Maxwell's equations and how wave propagation relates to intensity. Also, the polarization state is described in detail, as this is vital in understanding how electromagnetic fields react with hydrometeors in a precipitating environment.

1.2.1 The Wave Equation

Maxwell's equations provide the basis for the behavior of electromagnetic waves [8]. The plane wave solution for these equations express the mechanism by which electromagnetic waves propagate through an unbounded medium. Given a source-free, non-magnetic, lossy and homogeneous medium, the plane wave solution for Maxwell's equations are

$$\mathbf{E}(\mathbf{r}, t) = \mathbf{E_0} \mathrm{e}^{\mathrm{j}\mathbf{k}\cdot\mathbf{r} - \mathrm{j}wt}, \tag{1.1}$$

$$\mathbf{H}(\mathbf{r},t) = \mathbf{H_0} \mathrm{e}^{\mathrm{j}\mathbf{k}\cdot\mathbf{r}-\mathrm{j}wt}, \tag{1.2}$$

where $\mathbf{E}$ is the complex electric field, $\mathbf{H}$ is the complex magnetic field, and $\mathbf{E_0}$ and $\mathbf{H_0}$ are constant complex vectors. $\mathbf{k} = \mathbf{k}' + \mathrm{j}\mathbf{k}''$ is the complex wave vector, which describes the propagation properties of the wave, and $\mathbf{r}$ is the position vector. To satisfy the plane wave solution, Maxwell's equations take the form

$$\mathbf{k} \cdot \mathbf{E_0} = 0, \tag{1.3}$$

$$\mathbf{k} \cdot \mathbf{H_0} = 0, \tag{1.4}$$

$$\mathbf{k} \times \mathbf{E_0} = \omega\mu\mathbf{H_0}, \tag{1.5}$$

$$\mathbf{k} \times \mathbf{H_0} = -\omega\epsilon\mathbf{E_0}. \tag{1.6}$$

The intensity of energy flow is a quantity of interest in radiative transfer. The time average Poynting vector $\langle\mathbf{S}(\mathbf{r})\rangle$, defined as

$$\langle\mathbf{S}(\mathbf{r})\rangle = \frac{1}{2}\mathrm{Re}\left\{\langle\mathbf{E}(\mathbf{r})\rangle \times \langle\mathbf{H}^*(\mathbf{r})\rangle\right\}. \tag{1.7}$$

describes the flow of electromagnetic energy. When considering a homogeneous wave, (1.7) yields

$$\langle\mathbf{S}(\mathbf{r})\rangle = \frac{1}{2}\mathrm{Re}\left\{\sqrt{\frac{\epsilon}{\mu}}\right\} |\mathbf{E_0}|^2 \, \mathrm{e}^{-2\alpha\hat{\mathbf{n}}\cdot\mathbf{r}}\hat{\mathbf{n}}. \tag{1.8}$$

The absolute value of the time averaged Poynting vector, $I(\mathbf{r}) = |\langle\mathbf{S}(\mathbf{r})\rangle|$, is the irradiance. From (1.8),

$$I(\mathbf{r}) = I_0 \mathrm{e}^{-2\alpha\hat{\mathbf{n}}\cdot\mathbf{r}}, \tag{1.9}$$

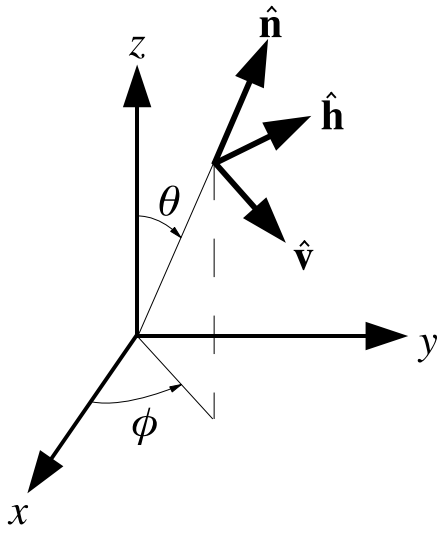

Figure 1.1: Coordinate system defining the direction of propagation and polarization.

where I_0 is the intensity at $\mathbf{r} = 0$ and $I(\mathbf{r})$ has units of W/m^2.

1.2.2 Wave Polarization

Another property of a plane wave that is of interest is its polarization state, for which the common notation is the Stokes vector [9], [10]. The complex electric field can be represented by a set of orthogonal polarizations of arbitrary orientation. Fig. 1.1 [9] displays this local coordinate system, with the plane of incidence defined by ϕ and the z-axis. By choosing the plane of incidence as a frame of reference, the vertical field, $\mathbf{E_v} = E_{0v}\hat{\mathbf{v}}$, denotes the field component that is parallel to this plane while the horizontal field, $\mathbf{E_h} = E_{0h}\hat{\mathbf{h}}$ refers to the perpendicular component, with $\hat{\mathbf{n}} = \hat{\mathbf{v}} \times \hat{\mathbf{h}}$.

For a transverse monochromatic electromagnetic wave traveling through a medium with constant and real ϵ, μ, and k described by (1.1), the Stokes vector is

$$\mathbf{I} = \begin{bmatrix} I \\ Q \\ U \\ V \end{bmatrix} = \frac{1}{2}\sqrt{\frac{\epsilon}{\mu}} \begin{bmatrix} E_{0v}E_{0v}^* + E_{0h}E_{0h}^* \\ E_{0v}E_{0v}^* - E_{0h}E_{0h}^* \\ -E_{0v}E_{0h}^* - E_{0h}E_{0v}^* \\ \mathrm{j}(E_{0h}E_{0v}^* - E_{0v}E_{0h}^*) \end{bmatrix} = \frac{1}{2}\sqrt{\frac{\epsilon}{\mu}} \begin{bmatrix} E_{0v}E_{0v}^* + E_{0h}E_{0h}^* \\ E_{0v}E_{0v}^* - E_{0h}E_{0h}^* \\ -2\mathrm{Re}(E_{0v}E_{0h}^*) \\ 2\mathrm{Im}(E_{0v}E_{0h}^*) \end{bmatrix}. \tag{1.10}$$

An alternate form, used widely by the microwave remote sensing community, is the modified Stokes vector

$$\mathbf{I}_{mod} = \begin{bmatrix} I_{0v} \\ I_{0h} \\ U \\ V \end{bmatrix} = \frac{1}{2}\sqrt{\frac{\epsilon}{\mu}} \begin{bmatrix} E_{0v}E_{0v}^* \\ E_{0h}E_{0h}^* \\ -2\mathrm{Re}(E_{0v}E_{0h}^*) \\ 2\mathrm{Im}(E_{0v}E_{0h}^*) \end{bmatrix}. \tag{1.11}$$

Using real, non-negative amplitudes a_v and a_h and phases δ_v and δ_h, the complex vertical and horizontal fields are

$$E_{0v} = a_v \mathrm{e}^{i\delta_v} \tag{1.12}$$

$$E_{0h} = a_h \mathrm{e}^{i\delta_h}. \tag{1.13}$$

Combining this phase and amplitude representation of the electric fields with (1.10), the four Stokes parameters are

$$I = a_v^2 + a_h^2 \tag{1.14}$$

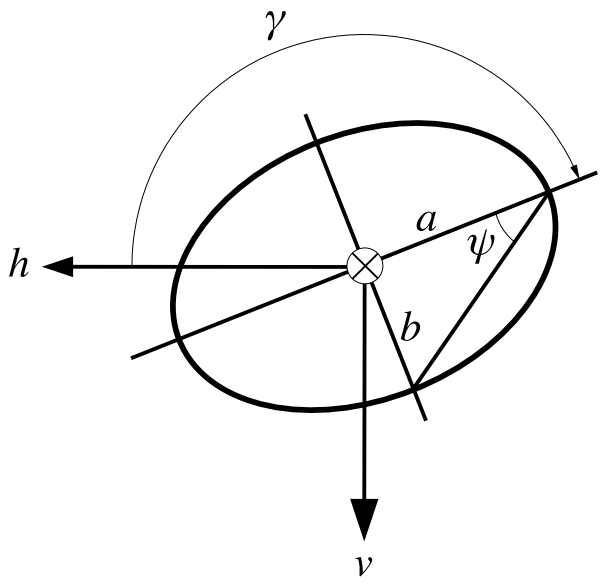

Figure 1.2: Polarization ellipse.

$$Q = a_v^2 - a_h^2 \tag{1.15}$$

$$U = -2a_v a_h cos(\delta_v - \delta_h) \tag{1.16}$$

$$V = 2a_v a_h sin(\delta_v - \delta_h). \tag{1.17}$$

The quantity $\frac{1}{2}\sqrt{\frac{\epsilon}{\mu}}$ is ignored for visual clarity, since the relative intensities are the primary quantity of interest.

While waves can be described by a specific polarization state, e.g., linearly polarized, the general description for polarization is that of an ellipse as in Fig. 1.2 [9]. The ellipsometric parameters for polarization are handedness, ellipticity, and azimuth. Handedness describes the rotation of the ellipse in time, i.e., right-handed polarization

describes a wave rotating clockwise when viewed propagating away from the observer. Ellipticity, $\arctan\psi$, is the ratio of the semi-minor axis to the semi-major axis and azimuth, γ, is the orientation of the semi-major axis with respect to the $h-$axis. Positive ψ corresponds to right-handed polarization, with negative denoting left. The Stokes parameters relate to the ellipsometric representation of an electromagnetic plane wave through the following relations:

$$I = a^2 \tag{1.18}$$

$$Q = -I\cos 2\psi\cos 2\gamma \tag{1.19}$$

$$U = I\cos 2\psi\sin 2\gamma \tag{1.20}$$

$$V = -I\sin 2\psi. \tag{1.21}$$

From these, the solutions for the ellipsometric parameters, in terms of the Stokes parameters, are

$$\tan 2\gamma = -\frac{U}{Q} \tag{1.22}$$

and

$$\tan 2\psi = -\frac{V}{\sqrt{Q^2+U^2}}. \tag{1.23}$$

These solutions are valid for $|\psi| = \pi/4$; therefore, $\cos 2\gamma$ must have the same sign as $-Q$. Also, from (1.23), negative V corresponds to right-handed polarization, and positive V to left. Since the values of Q and U depend on the alignment of the basis vectors $\hat{\mathbf{v}}$ and $\hat{\mathbf{h}}$, a rotation of the basis vectors, as in Fig. 1.3 [10], results in

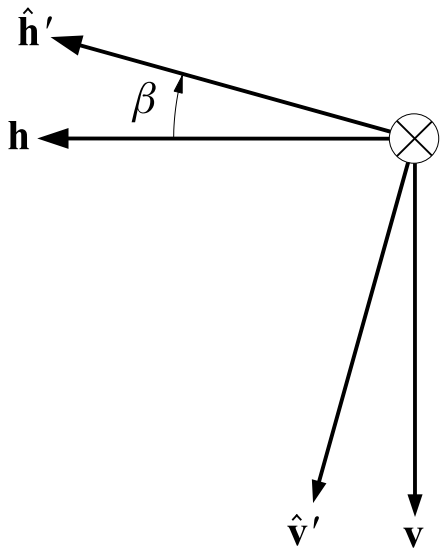

Figure 1.3: Basis vector rotation, $\hat{\mathbf{n}}$ pointing away from observer.

a transformation of the Stokes parameters. Given the rotated vectors $\hat{\mathbf{v}}'$ and $\hat{\mathbf{h}}'$, the transformed Stokes vector is

$$\begin{bmatrix} I' \\ Q' \\ U' \\ V' \end{bmatrix} = \begin{bmatrix} 1 & 0 & 0 & 0 \\ 0 & \cos 2\beta & -\sin 2\beta & 0 \\ 0 & \sin 2\beta & \cos 2\beta & 0 \\ 0 & 0 & 0 & 1 \end{bmatrix} \begin{bmatrix} I \\ Q \\ U \\ V \end{bmatrix} \tag{1.24}$$

The preceding equations describe a monochromatic beam, i.e., one where $\mathbf{E_0}$, and, thusly, a_v, a_h, δ_v, and δ_h, do not fluctuate in time. Many waves, however, exhibit small fluctuations over long time intervals with respect to the period $2\pi/\omega$. Such a wave is called a quasi-monochromatic beam. Detectors such as radiometers measure

the time-averaged Stokes intensities over such periods of time; therefore, the set of equations that represents the time-averaged Stokes vector is

$$I = \langle E_{0v}E_{0v}^* + E_{0v}E_{0v}^* \rangle = \left\langle a_v^2 + a_h^2 \right\rangle, \tag{1.25}$$

$$Q = \langle E_{0v}E_{0v}^* - E_{0v}E_{0v}^* \rangle = \left\langle a_v^2 - a_h^2 \right\rangle, \tag{1.26}$$

$$U = -\langle E_{0v}E_{0h}^* + E_{0h}E_{0v}^* \rangle = -2\langle a_v a_h \cos(\delta_v - \delta_h) \rangle, \tag{1.27}$$

$$V = \mathrm{j}\langle E_{0h}E_{0v}^* - E_{0v}E_{0h}^* \rangle = 2\langle a_v a_h \sin(\delta_v - \delta_h) \rangle. \tag{1.28}$$

From (1.25) - (1.28),

$$Q^2 + U^2 + V^2 = I^2 - 4\left[\left\langle a_v^2 \right\rangle \left\langle a_h^2 \right\rangle - \langle a_v a_h \cos(\delta_v - \delta_h) \rangle^2 - \langle a_v a_h \sin(\delta_v - \delta_h) \rangle^2\right]; \tag{1.29}$$

therefore,

$$I^2 \geq Q^2 + U^2 + V^2. \tag{1.30}$$

If the ratio a_v/a_h and the phase difference $\delta_v - \delta_h$ are time-invariant, then E_v and E_h are completely correlated and the beam is considered to be completely polarized, with $I^2 = Q^2 + U^2 + V^2$. The monochromatic beam is a special case of the completely polarized beam. When E_v and E_h are completely uncorrelated, the beam is completely unpolarized–as in natural light–and $Q = U = V = 0$. If E_v and E_h are partially correlated, the beam is partially polarized.

With a full description of propagating electromagnetic radiation, the interaction of this radiation with atmospheric constituents can be derived. The next two chapters

explain these interactions and give a method for determining the resultant electromagnetic fields for certain idealized situations applicable to precipitating hydrometeors.

CHAPTER 2
RADIATIVE TRANSFER THEORY

When a plane wave, traveling through some homogeneous medium, is incident upon a particle of finite size with a refractive index different than that of the the surrounding medium, the presence of the particle alters the total electromagnetic field [9], [10]. Many applications of scattering theory, however, require the consideration of a large number of particles, such as clouds or volumes of falling hydrometeors (rain, snow, graupel). Since the solution to Maxwell's equations for such situations is cumbersome and computationally inefficient, application of scattering theory to a collection of particles requires extending the understanding of absorption, emission, and scattering of a single particle.

Section 2.1 outlines the interaction of plane electromagnetic waves with a single particle. Equations that describe scattering and extinction are explained, as is the phenomena of Planck emission. Although gas absorption is the interaction of electromagnetic radiation with trace gas molecules in the atmosphere, it is treated individually in Section 2.2. Section 2.3 discusses methods for simplifying the scattering, absorption and emission by a collection of particles under certain conditions, including the phenomenological derivation of the radiative transfer equation.

2.1 Single Particle Interactions

A single particle can be described as a collection of electric charges that, when excited by an incident wave, oscillates at the same frequency as the wave and radiates secondary electromagnetic waves through a process known as elastic scattering. The total wave, then, is the vector sum of the incident and scattered waves. If the oscillations of the elementary constituents of the particle are not in phase, then the object dissipates some of the incident energy through absorption. The total reduction of the incident field by both scattering and absorption is termed extinction. The particle may also be dichroic, in that the extinction may not be uniform for all polarization components of the incident wave, thereby causing a change in polarization state. Additionally, all particles above absolute zero radiate energy at all frequencies and in all directions–a process known as thermal emission.

2.1.1 Volume Wave Equation

To determine the total electromagnetic field induced by the interaction of a plane wave incident on a single particle, space is divided into two distinct volumes [9]. The first is a semi-infinite, non-absorbing, homogeneous, linear, and isotropic medium with wave number k_1, not including the space inside the scattering particle. The

second is the volume inside the finite scattering element, which is linear and isotropic, but may not be homogeneous and has a wave number $k_2(\mathbf{r})$. If only a non-magnetic medium is considered, the vector wave equations for $\mathbf{r}$ outside and inside the scatterer, respectively, are

$$\nabla \times \nabla \times \mathbf{E}(\mathbf{r}) - k_1^2 \mathbf{E}(\mathbf{r}) = 0 \tag{2.1}$$

$$\nabla \times \nabla \times \mathbf{E}(\mathbf{r}) - k_2^2(\mathbf{r}) \mathbf{E}(\mathbf{r}) = 0. \tag{2.2}$$

Combining (2.1) and (2.2) results in the inhomogeneous differential equation

$$\nabla^2 \times \mathbf{E}(\mathbf{r}) - k_1^2 \mathbf{E}(\mathbf{r}) = k_1^2 \left[\frac{k_M}{k_1} - 1 \right] \mathbf{E}(\mathbf{r}) \tag{2.3}$$

where k_M is k_1 outside of the scattering particle and $k_2(\mathbf{r})$ inside the scattering particle. Using superposition, the inhomogeneous differential equation may be separated into homogeneous and inhomogeneous parts. The homogeneous component of (2.3) refers to the incident field. The inhomogeneous component may be solved using the dyadic Green's function [11], [12]. The total field, therefore, is

$$\begin{aligned} \mathbf{E}(\mathbf{r}) &= \mathbf{E}^i(\mathbf{r}) + \mathbf{E}^s(\mathbf{r}) \\ &= \mathbf{E}^i(\mathbf{r}) + k_1^2 \int_V \mathrm{d}\mathbf{r}' \bar{\mathbf{G}}(\mathbf{r}, \mathbf{r}') \cdot \mathbf{E}(\mathbf{r}') \left[\frac{k_2(\mathbf{r})}{k_1} - 1 \right]. \end{aligned} \tag{2.4}$$

$\mathbf{E}^i$ is the incident electric field, $\mathbf{E}^s$ is the scattered electric field, $\bar{\mathbf{G}}(\mathbf{r}, \mathbf{r}')$ is the dyadic Green's function, the argument of the integral is integrated over the internal volume of the scattering element, and $\mathbf{r}$ is within the entire space considered. Using an

iterative method, the internal field relates to the incident field in terms of the dyadic transitional operator $\bar{\mathbf{T}}$ [12]:

$$\mathbf{E}(\mathbf{r}) = \mathbf{E}^i(\mathbf{r}) + \int_V \mathrm{d}\mathbf{r}' \bar{\mathbf{G}}(\mathbf{r}, \mathbf{r}') \int_V \mathrm{d}\mathbf{r}'' \bar{\mathbf{T}}(\mathbf{r}', \mathbf{r}'') \cdot \mathbf{E}(\mathbf{r}''). \tag{2.5}$$

Most scattering applications require the relationship between the incident field and the scattered field in the far-field region. Given that the incident plane wave is of the form

$$\mathbf{E}^i(\mathbf{r}) = E_0^i \mathrm{e}^{\mathrm{j}k_1 \hat{\mathbf{n}}^i \cdot \mathbf{r}}, \tag{2.6}$$

the scattered field, in the far-field region, is described as

$$\mathbf{E}^s(r\hat{\mathbf{n}}^s) = \frac{\mathrm{e}^{\mathrm{j}k_1 r}}{r} \bar{\mathbf{A}}(\hat{\mathbf{n}}^s, \hat{\mathbf{n}}^i) \cdot E_0^i, \tag{2.7}$$

where $\hat{\mathbf{n}}^s = \hat{\mathbf{r}}$ and $\bar{\mathbf{A}}$ is the scattering dyadic. The scattering dyadic is a function of the dyadic transitional operator:

$$\bar{\mathbf{A}}(\hat{\mathbf{n}}^s, \hat{\mathbf{n}}^i) = \frac{1}{4\pi}(\bar{\mathbf{I}} - \hat{\mathbf{n}}^s \otimes \hat{\mathbf{n}}^s) \cdot \int_V \mathrm{d}\mathbf{r}' \mathrm{e}^{-\mathrm{j}k_1 \hat{\mathbf{n}}^s \cdot \mathbf{r}'} \times \int_V \mathrm{d}\mathbf{r}'' \bar{\mathbf{T}}(\mathbf{r}', \mathbf{r}'') \mathrm{e}^{\mathrm{j}k_1 \hat{\mathbf{n}}^i \cdot \mathbf{r}''}, \tag{2.8}$$

where the dyadic product $\mathbf{x} \otimes \mathbf{y}$ gives the dyad of the vectors $\mathbf{x}$ and $\mathbf{y}$. $\bar{\mathbf{I}} = \hat{\mathbf{r}} \otimes \hat{\mathbf{r}} + \hat{\boldsymbol{\theta}} \otimes \hat{\boldsymbol{\theta}} + \hat{\boldsymbol{\phi}} \otimes \hat{\boldsymbol{\phi}}$ is the identity dyadic in the spherical coordinate system, implying that $\bar{\mathbf{I}} - \hat{\mathbf{r}} \otimes \hat{\mathbf{r}}$ from (2.8) imposes the condition that the scattering dyadic is transverse to the scattered direction. In addition, the scattering dyadic is also transverse to the incident direction.

2.1.2 Stokes Scattering Parameters

Due its transverse nature, the scattering dyadic defined in the previous section only has four independent elements, which may be represented by the amplitude scattering matrix. The 2×2 amplitude scattering matrix accounts for the transformation of the h- and v-components of the incident plane wave (as in Fig. 1.1) to those of the scattered spherical wave. This relationship between incident and scattered plane wave is

$$\begin{bmatrix} E_v^s(r\hat{\mathbf{n}}) \\ E_h^s(r\hat{\mathbf{n}}) \end{bmatrix} = \frac{\mathrm{e}^{\mathrm{j}k_1 r}}{r} \begin{bmatrix} S_{11} & S_{12} \\ S_{21} & S_{22} \end{bmatrix} \begin{bmatrix} E_{0v}^i \\ E_{0h}^i \end{bmatrix}, \tag{2.9}$$

where the individual matrix elements are related to the scattering dyadic by

$$S_{11} = \hat{\mathbf{v}}^s \cdot \bar{\mathbf{A}} \cdot \hat{\mathbf{v}}^i, \tag{2.10}$$

$$S_{12} = \hat{\mathbf{v}}^s \cdot \bar{\mathbf{A}} \cdot \hat{\mathbf{h}}^i, \tag{2.11}$$

$$S_{21} = \hat{\mathbf{h}}^s \cdot \bar{\mathbf{A}} \cdot \hat{\mathbf{v}}^i, \tag{2.12}$$

$$S_{22} = \hat{\mathbf{h}}^s \cdot \bar{\mathbf{A}} \cdot \hat{\mathbf{h}}^i. \tag{2.13}$$

The phase matrix $\mathbf{Z}$ gives the transformation between the scattered Stokes vector and the incident Stokes vector for $\hat{\mathbf{n}}^s \neq \hat{\mathbf{n}}^i$:

$$\mathbf{I}^s(r\hat{\mathbf{n}}^s) = \frac{1}{r^2}\mathbf{Z}(\hat{\mathbf{n}}^s, \hat{\mathbf{n}}^i)\mathbf{I}^i, \tag{2.14}$$

The elements of the amplitude scattering matrix define the phase matrix:

$$Z_{11} = \tfrac{1}{2}\left(|S_{11}|^2 + |S_{12}|^2 + |S_{21}|^2 + |S_{22}|^2\right), \tag{2.15}$$

$$Z_{12} = \tfrac{1}{2}\left(|S_{11}|^2 - |S_{12}|^2 + |S_{21}|^2 - |S_{22}|^2\right), \tag{2.16}$$

$$Z_{13} = -\mathrm{Re}\left(S_{11}S_{12}^* + S_{22}S_{21}^*\right), \tag{2.17}$$

$$Z_{14} = -\mathrm{Im}\left(S_{11}S_{12}^* - S_{22}S_{21}^*\right), \tag{2.18}$$

$$Z_{21} = \tfrac{1}{2}\left(|S_{11}|^2 + |S_{12}|^2 - |S_{21}|^2 - |S_{22}|^2\right), \tag{2.19}$$

$$Z_{22} = \tfrac{1}{2}\left(|S_{11}|^2 - |S_{12}|^2 - |S_{21}|^2 + |S_{22}|^2\right), \tag{2.20}$$

$$Z_{23} = -\mathrm{Re}\left(S_{11}S_{12}^* - S_{22}S_{21}^*\right), \tag{2.21}$$

$$Z_{24} = -\mathrm{Im}\left(S_{11}S_{12}^* + S_{22}S_{21}^*\right), \tag{2.22}$$

$$Z_{31} = -\mathrm{Re}\left(S_{11}S_{21}^* + S_{22}S_{12}^*\right), \tag{2.23}$$

$$Z_{32} = -\mathrm{Re}\left(S_{11}S_{21}^* - S_{22}S_{12}^*\right), \tag{2.24}$$

$$Z_{33} = \mathrm{Re}\left(S_{11}S_{22}^* + S_{12}S_{21}^*\right), \tag{2.25}$$

$$Z_{34} = \mathrm{Im}\left(S_{11}S_{22}^* + S_{21}S_{12}^*\right), \tag{2.26}$$

$$Z_{41} = -\mathrm{Im}\left(S_{21}S_{11}^* + S_{22}S_{12}^*\right), \tag{2.27}$$

$$Z_{42} = -\mathrm{Im}\left(S_{21}S_{11}^* - S_{22}S_{12}^*\right), \tag{2.28}$$

$$Z_{43} = \mathrm{Im}\left(S_{22}S_{11}^* - S_{12}S_{21}^*\right), \tag{2.29}$$

$$Z_{44} = \mathrm{Re}\left(S_{22}S_{11}^* - S_{12}S_{21}^*\right). \tag{2.30}$$

For the special case of $\hat{\mathbf{n}}^s = \hat{\mathbf{n}}^i$, i.e., exact forward scattering, the 4×4 extinction matrix $\mathbf{K}$ describes the attenuation of the forward propagating wave due to scattering by a particle. The resultant Stokes vector over a small surface element ΔS perpendicular to $\hat{\mathbf{n}}^i$, due to extinction, is

$$\mathbf{I}(r\hat{\mathbf{n}}^i)\Delta S = \mathbf{I}^i \Delta S - \mathbf{K}(\hat{\mathbf{n}}^i)\mathbf{I}^i + O(r^{-2}), \tag{2.31}$$

where $O(r^{-2})$ describes the component of the elastically scattered spherical wave, proportional to $\frac{1}{r^2}$, propagating in the direction of $\hat{\mathbf{n}}^i$. As with the phase matrix, the elements of the amplitude scattering matrix define the extinction matrix:

$$K_{ii} = \frac{2\pi}{k_1}\mathrm{Im}(S_{11} + S_{22}), \qquad i = 1, 2, 3, 4, \tag{2.32}$$

$$K_{12} = K_{21} = \frac{2\pi}{k_1}\mathrm{Im}(S_{11} - S_{22}), \tag{2.33}$$

$$K_{13} = K_{31} = -\frac{2\pi}{k_1}\mathrm{Im}(S_{12} + S_{21}), \tag{2.34}$$

$$K_{14} = K_{41} = \frac{2\pi}{k_1}\mathrm{Re}(S_{21} - S_{12}), \tag{2.35}$$

$$K_{23} = -K_{32} = \frac{2\pi}{k_1}\mathrm{Im}(S_{21} - S_{12}), \tag{2.36}$$

$$K_{24} = -K_{42} = -\frac{2\pi}{k_1}\mathrm{Re}(S_{12} + S_{21}), \tag{2.37}$$

$$K_{34} = -K_{43} = \frac{2\pi}{k_1}\mathrm{Re}(S_{22} - S_{11}). \tag{2.38}$$

2.1.3 Optical Cross Sections

With a mathematical basis for the Stokes vector in the far-field region, it is possible to quantify the power removed from the electromagnetic field due to scattering and absorption. Optical cross sections are the ratios of the power removed by absorption and/or scattering to the incident energy flux. If the medium in which the object lies is non-absorbing, then the W_{abs} is solely the power absorbed by the particle, and can be defined as the combination of three terms: $W_{abs} = W_{inc} - W_{sca} + W_{ext}$, where

$$W_{inc} = -\int_S \mathrm{d}S\langle \mathbf{S}^i(\mathbf{r})\rangle \cdot \hat{\mathbf{r}}, \qquad W_{sca} = -\int_S \mathrm{d}S\langle \mathbf{S}^s(\mathbf{r})\rangle \cdot \hat{\mathbf{r}},$$
$$W_{ext} = -\int_S \mathrm{d}S\langle \mathbf{S}^e(\mathbf{r})\rangle \cdot \hat{\mathbf{r}}, \tag{2.39}$$

where S is the surface area of an imaginary sphere surrounding the scattering element. Since the surrounding medium is non-absorbing and $\mathbf{S}^i(\mathbf{r})$ is constant and independent of $\mathbf{r}$, W_{inc} vanishes; therefore, W_{ext} is the sum of the scattered and absorbed power, i.e.,

$$W_{ext} = W_{sca} + W_{abs} \tag{2.40}$$

with $W_{abs} \geq 0$, as the volume inside the sphere is considered to not be creating energy.

From (2.39), and knowledge that the cross section is the ratio of power to incident energy flux, the scattering cross is

$$C_{sca} = \frac{1}{I^i r^2}\int_S dS\left[Z_{11}(\hat{\mathbf{r}},\hat{\mathbf{n}}^i)I^i + Z_{12}(\hat{\mathbf{r}},\hat{\mathbf{n}}^i)Q^i + Z_{13}(\hat{\mathbf{r}},\hat{\mathbf{n}}^i)U^i + Z_{14}(\hat{\mathbf{r}},\hat{\mathbf{n}}^i)V^i\right], \tag{2.41}$$

and the extinction cross is

$$C_{ext} = \frac{1}{I^i}\left[K_{11}(\hat{n}^i)I^i + K_{12}(\hat{n}^i)Q^i + K_{13}(\hat{n}^i)U^i + K_{14}(\hat{n}^i)V^i\right]. \tag{2.42}$$

Therefore, using (2.40), the absorption cross section is

$$C_{abs} = C_{ext} - C_{sca}. \tag{2.43}$$

The cross sections are real-valued and positive, all with dimensions of area.

$$\bar{\omega} = \frac{C_{sca}}{C_{ext}} \tag{2.44}$$

is the single scattering albedo, often used as the probability of a photon being scattered by the element instead of being absorbed.

For a scattering element with cross-sectional area G projected on ΔS, the extinction, absorption and scattering efficiencies are, respectively,

$$Q_{ext} = \frac{C_{ext}}{G}, \qquad Q_{sca} = \frac{C_{sca}}{G}, \qquad Q_{abs} = \frac{C_{abs}}{G}. \tag{2.45}$$

2.1.4 Planck Emission

Besides absorbing and scattering incident radiation, all particles with temperature above absolute zero ($T > 0K$) also emit energy at at all frequencies. Assume that the particle is contained within an isotropic, homogeneous and unpolarized cavity, where the particle and the cavity are in thermodynamic equilibrium at some temperature T.

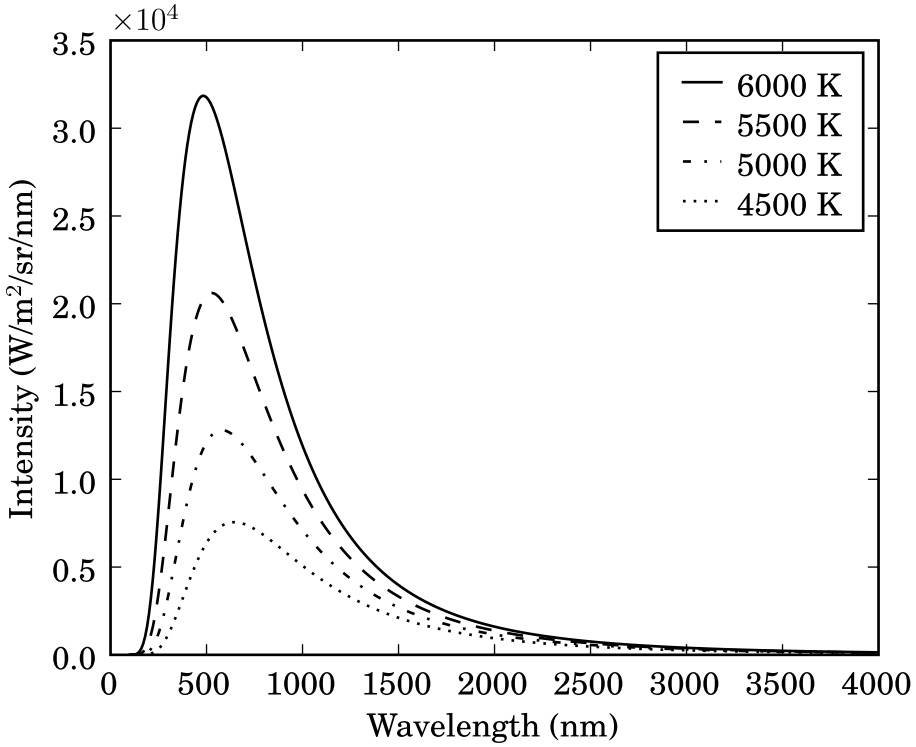

Figure 2.1: Planck black body distribution including visible light spectrum.

The incoherent intensity in all directions within the cavity is the Planck blackbody distribution, Fig. 2.1,

$$I_{T_b}(T,\lambda) = \frac{2hc^2}{\lambda^5\left[e^{\frac{hc}{k_B\lambda T}} - 1\right]} \tag{2.46}$$

where h denotes Planck's constant, c is the free-space speed of light, and k_B is Boltzmann's constant. A surface element ΔS with a solid angle field of view $\Delta\Omega$ is considered at some distance r, such that ΔS is in the far-field region of the scattering element, but less than a distance of $\sqrt{\Delta S \Delta\Omega}$. Without the particle, the black-

body Stokes column vector, $\mathbf{I}_{T_b}(T,\omega)$, is fully unpolarized, so $I = I_{T_b}(T,\omega)$, and $Q = U = V = 0$; therefore, the signal across ΔS is

$$\mathbf{I}_{T_b}(T,\omega)\Delta S\Delta\Omega. \tag{2.47}$$

When considering the presence of the scattering particle, which absorbs, emits and scatters energy, the signal across ΔS is

$$\begin{aligned}&\mathbf{I}_{T_b}(T,\omega)\Delta S\Delta\Omega - \mathbf{K}(\hat{\mathbf{r}},\omega)\mathbf{I}_{T_b}(T,\omega)\Delta\Omega+\\&\mathbf{K_a}(\hat{\mathbf{r}},T,\omega)I_{T_b}(T,\omega)\Delta\Omega + \Delta\Omega\int_{4\pi}\mathrm{d}\hat{\mathbf{r}}'\mathbf{Z}(\hat{\mathbf{r}},\hat{\mathbf{r}}',\omega)\mathbf{I}_{T_b}(T,\omega)\end{aligned} \tag{2.48}$$

where $\mathbf{K_a}(\hat{\mathbf{r}},T,\omega)$ is the Stokes absorption (emissivity) column vector. Due to the condition that the cavity and the particle are in thermodynamic equilibrium, (2.47) and (2.48) are equivalent; therefore, the ith element of $\mathbf{K_a}$ is a function of the ith elements of the first columns of the extinction and phase matrices:

$$K_{ai}(\hat{\mathbf{r}},T,\omega) = K_{i1}(\hat{\mathbf{r}},\omega) - \int_{4\pi}\mathrm{d}\hat{\mathbf{r}}'Z_{i1}(\hat{\mathbf{r}},\hat{\mathbf{r}}',\omega), \qquad i = 1,2,3,4. \tag{2.49}$$

The relation holds regardless of whether a particle is in thermodynamic equilibrium with its environment or not.

2.2 Gas Absorption

Absorption and emission are not constrained to appreciable particles, as detailed in Section 2.1.4. Absorption and emission also occur at a molecular level. With respect

to the scope of this research, emission and absorption by gasses in the atmosphere are isotropic and non-dichroic; however, they are considered for completeness when performing radiative calculations. Since gas absorption does not affect polarization, only a general description is given.

Quantum energy changes of trace gas molecules result in gas absorption and emission spectra [7]. The three energy mechanisms that contribute to this phenomenon are rotational energy, where a molecule rotates about an axis through its center of gravity; vibrational energy, with which the atomic bonds stretch and contract; and electronic energy, when electrons change energy state. Molecules gain energy by absorbing photons, and lose energy by emitting photons. Pure rotational transitions correspond to maximum wavelengths on the order of 1 cm, and are in the microwave and far-infrared spectra. Vibrational transitions occur at wavelengths below about 15 μm, the intermediate infrared spectrum, and are always coupled with rotational changes. Electron energy changes require large amounts of energy usually correspond to the ultraviolet or visible spectra.

While emission and absorption of photons should be monochromatic, external forces and loss of energy result in finite widths of spectral lines, a phenomenon known as line broadening. Energy loss (natural broadening), is usually negligible. In the lower atmosphere pressure forces collisions between absorbing and non-absorbing molecules

(pressure broadening), while in the upper atmosphere there is a Doppler effect corresponding to the thermal velocities of atoms and molecules (Doppler broadening).

The absorption vector for a gas reduces to a scalar absorption coefficient. In the microwave region scattering is neglected, and the extinction matrix is diagonal, with the diagonal elements equal to the scalar absorption coefficient. By not considering scattering, there is no need to calculate a phase matrix. Therefore, emission is unpolarized and absorption (attenuation) is constant for all Stokes parameters, with no cross-polarization effects.

2.3 The Consideration of Multiple Particles

The equations developed in Section 2.1 describe the the scattering, absorption, and emission of an individual particle. Useful application of scattering theory, however, requires the consideration of a large number of particles. Solving Maxwell's equations for large numbers of particles becomes unwieldy and computation can be prohibitive. Under certain simplifying assumptions, however, a large group of scattering particles can be considered a single medium.

2.3.1 Single Scattering Approximation

The computation of scattering, absorption and emission for a collection of particles is greatly simplified when each of the particles are positioned in the far-field regions of each other and of the observation point. Under these conditions, only the initial scattering events are considered significant, allowing subsequent scattering events to be ignored. This scenario is the single scattering approximation. To illustrate this example, consider a small volume of linear dimension l consisting of N particles. N is sufficiently small that the spacing between particles is much greater than either the particle size or the incident radiation wavelength. Also, the spacing is such that multiple scattering is negligible, which is equivalent to $N\langle C_{sca}\rangle/l^2 \ll 1$. Additionally, the positions of the particles are sufficiently random such that there is no coherency between the scattered waves. Given these conditions, the total field scattered by the volume, at some large distance r, is the vector sum of the partial scattered fields:

$$\mathbf{E}^s(\mathbf{r}) = \sum_{n=1}^{N} \mathbf{E}_n^s(\mathbf{r}) \tag{2.50}$$

where $\mathbf{r}$ is the position vector originating at the geometric center O of the volume. Additionally, the partial scattered fields, using equation (2.9), are

$$\begin{bmatrix} [E_n^s]_v(\mathbf{r}) \\ [E_n^s]_h(\mathbf{r}) \end{bmatrix} = \frac{e^{jk_1 r}}{r} e^{j\Delta_n} \begin{bmatrix} S_{11n} & S_{12n} \\ S_{21n} & S_{22n} \end{bmatrix} \begin{bmatrix} E_{0v}^i \\ E_{0h}^i \end{bmatrix} \tag{2.51}$$

where the phase Δ_n is

$$\Delta_n = k_1 \mathbf{r}_{On} \cdot (\hat{\mathbf{n}}^i - \hat{\mathbf{r}}) \tag{2.52}$$

and $\mathbf{r}_{On}$ is the vector from O to the nth particle. Thus, the entire volume element represents a single scatterer. The elements of the total amplitude scattering matrix are

$$S_{ik} = \sum_{n=1}^{N} \mathrm{e}^{\mathrm{j}\Delta_n} S_{ikn}, \qquad i,k = 1,2. \tag{2.53}$$

As $\Delta_n \to 0$ in the forward scattering direction, the total extinction matrix is

$$\mathbf{K} = \sum_{n=1}^{N} \mathbf{K} = N \langle \mathbf{K} \rangle \tag{2.54}$$

where $\langle \mathbf{K} \rangle$ is the ensemble-averaged extinction matrix. The total extinction cross section is, therefore,

$$C_{ext} = \sum_{n=1}^{N} (C_{ext})_n = N \langle C_{ext} \rangle . \tag{2.55}$$

Similarly, the total phase matrix for the volume is

$$\mathbf{Z} = \sum_{n=1}^{N} \mathbf{Z} = N \langle \mathbf{Z} \rangle \tag{2.56}$$

where $\langle \mathbf{Z} \rangle$ is the ensemble-averaged extinction matrix. The scattering and absorption cross sections are

$$C_{sca} = \sum_{n=1}^{N} (C_{sca})_n = N \langle C_{sca} \rangle \tag{2.57}$$

and

$$C_{abs} = \sum_{n=1}^{N} (C_{abs})_n = N \langle C_{abs} \rangle . \tag{2.58}$$

Finally, the total absorption vector for the observed volume is

$$\mathbf{K_a} = \sum_{n=1}^{N} \mathbf{K_a} = N \langle \mathbf{K_a} \rangle \tag{2.59}$$

where $\langle \mathbf{K_a} \rangle$ is the ensemble-averaged absorption vector.

2.3.2 The Radiative Transfer Equation

In many cases, N becomes large enough to violate the condition $N \langle C_{sca} \rangle / l^2 \ll 1$, thus rendering the single scattering approximation invalid. While the individual particles are still in the far-field region with respect to each other, multiple scattering events must now be considered. Also, while the observation point may be in the far-field region of each of the individual particles, it may not be in the far-field region of the scattering volume; therefore, scattered radiation may be sensed from multiple directions. One method for quantifying the scattering, absorption, and emission of an large collection of different particles is the radiative transfer equation. Radiative transfer describes the phenomenon of radiation propagating through a medium consisting of randomly distributed particles. Instead of solving Maxwell's equations for the multiple interactions of electromagnetic waves with the particles within a volume, radiative transfer theory uses energy conservation to model the transport of radiation through the considered medium [7], [12], [13]. To illustrate this process, the scalar radiative transfer equation is derived first and is then extended to the Stokes vector.

Radiative transfer deals with the differential radiant energy. The differential energy over the angular frequency interval ω to $\omega + d\omega$ is a function of the monochromatic intensity:

$$dE(\mathbf{r}, \hat{\mathbf{n}}, \omega) = I(\mathbf{r}, \hat{\mathbf{n}}, \omega) \cos\theta \, \mathrm{d}S\mathrm{d}\Omega\mathrm{d}\omega\mathrm{d}t \tag{2.60}$$

where $\cos\theta dS$ and $d\Omega$ are the surface area element and the solid angle, respectively, over which dE is being considered. The intensity is, therefore,

$$I(\mathbf{r}, \hat{\mathbf{n}}, \omega) = \frac{dE(\mathbf{r}, \hat{\mathbf{n}}, \omega)}{\cos\theta \, \mathrm{d}S\mathrm{d}\Omega\mathrm{d}\omega\mathrm{d}t}. \tag{2.61}$$

The intensity has units of energy per time (or power) per area per solid angle per frequency. When passing through a volume with unit cross section and length ds, the total number of particles within the volume is $N_0(\mathbf{r})ds$, where N_0 is the particle number density. The change in intensity $dI(\mathbf{r}, \hat{\mathbf{n}}, \omega)$ consists of contributions from scattering, absorption and emission. The loss due to scattering and absorption, or extinction, is

$$\mathrm{d}I(\mathbf{r}, \hat{\mathbf{n}}, \omega) = -\mathrm{d}sN_0(\mathbf{r}) \langle C_{ext} \rangle I(\mathbf{r}, \hat{\mathbf{n}}, \omega) \tag{2.62}$$

Emission from each of the particles increases the specific intensity. Comparing (2.49) with (2.41), (2.42), and (2.43) shows that the scalar analog to the absorption (emissivity) column vector is the absorption cross section. Therefore, the change in specific intensity due to the emission particles is

$$\mathrm{d}I(\mathbf{r}, \hat{\mathbf{n}}, \omega) = \mathrm{d}sN_0(\mathbf{r}) \langle C_{abs} \rangle I_{T_b}(T, \omega). \tag{2.63}$$

In addition to emission contributions there is also an increase in the specific intensity from elastic scattering in the direction of propagation. The scalar analog for the phase matrix is element $Z_{11}(\mathbf{r}, \hat{\mathbf{n}}, \omega)$ of the phase matrix. The increase in specific intensity from scattering is, then,

$$\mathrm{d}I(\mathbf{r}, \hat{\mathbf{n}}, \omega) = \mathrm{d}sN_0(\mathbf{r}) \int_{4\pi} \mathrm{d}\hat{\mathbf{n}}' \left\langle Z_{11}(\mathbf{r}, \hat{\mathbf{n}}, \hat{\mathbf{n}}', \omega) \right\rangle I(\mathbf{r}, \hat{\mathbf{n}}, \omega). \tag{2.64}$$

Combining each of the contributions to the specific intensity, the scalar radiative transfer equation is then

$$\begin{aligned} \frac{\mathrm{d}}{\mathrm{d}s} I(\mathbf{r}, \hat{\mathbf{n}}, \omega) = & - N_0(\mathbf{r}) \left\langle C_{ext} \right\rangle I(\mathbf{r}, \hat{\mathbf{n}}, \omega) \\ & + N_0(\mathbf{r}) \left\langle C_{abs} \right\rangle I_{T_b}(T, \omega) \\ & + N_0(\mathbf{r}) \int_{4\pi} \mathrm{d}\hat{\mathbf{n}}' \left\langle Z_{11}(\mathbf{r}, \hat{\mathbf{n}}, \hat{\mathbf{n}}', \omega) \right\rangle I(\mathbf{r}, \hat{\mathbf{n}}, \omega). \end{aligned} \tag{2.65}$$

The scalar radiative transfer equation ignores dichroism and, therefore, applies to scenarios where polarization effects are not present or may be ignored. One such application is the extinction and emission of gaseous atmospheric constituents like water vapor.

When the scattering properties of a particle or a medium depend on incident and/or scattering directions, the relationship between the components of the Stokes vector governs the intensity of the electromagnetic radiation that flows through the medium. Such applications require the consideration of vector radiative transfer. The scalar radiative transfer equation extends easily to vector applications through the incoherent

addition of the Stokes parameters:

$$\begin{aligned}\frac{\mathrm{d}}{\mathrm{d}s}\mathbf{I}(\mathbf{r},\hat{\mathbf{n}},\omega) = &- N_0(\mathbf{r})\,\langle\mathbf{K}(\mathbf{r},\hat{\mathbf{n}},\omega)\rangle\,\mathbf{I}(\mathbf{r},\hat{\mathbf{n}},\omega)\\ &+ N_0(\mathbf{r})\,\langle\mathbf{K_a}(\mathbf{r},\hat{\mathbf{n}},\omega)\rangle\,I_{T_b}(T,\omega)\\ &+ N_0(\mathbf{r})\int_{4\pi}\mathrm{d}\hat{\mathbf{n}}'\,\langle\mathbf{Z}(\mathbf{r},\hat{\mathbf{n}},\hat{\mathbf{n}}',\omega)\rangle\,\mathbf{I}(\mathbf{r},\hat{\mathbf{n}},\omega).\end{aligned} \tag{2.66}$$

The processes of interaction between single particles or groups of particles is important in understanding how these particles affect incident radiation. However, (2.8) requires a solution for these phenomena to have any quantitative relevance. Numerous solutions exist to calculate the scattered fields given the incident fields. The following chapter outlines one relevant and computationally efficient solution–the T-matrix method.

CHAPTER 3
PARTICLE SCATTERING SOLUTIONS

The ability to perform radiative transfer calculations requires an accurate and efficient method of solving for the scattering dyadic. Two methods are available to generate the scattering and absorption characteristics of particles: analytical methods and experimental measurements. Experiments many times are difficult to interpret, yield incomplete results, and tend to be expensive [9]; therefore, measured scattering characteristics are beyond the scope of the research. Instead, this study utilizes analytically and numerically derived scattering parameters. This chapter describes the methods used to calculate the scattering, absorption, and emission characteristics of a few types of collections of particles: spherical particles, randomly oriented nonspherical particles, and horizontally aligned particles. This chapter also explains how these calculations will effect the Stokes parameters.

3.1 Transfer Matrix Method

At the turn of the 20th century, Lorenz, Mie and others independently derived the scattering solution for an isotropic, homogeneous sphere. This method is referred to as Lorenz-Mie (or Mie) Theory. Spheres are useful for approximating particles when

polarization effects are either insignificant or may be ignored. In the case of nonspherical particles, such as rain drops and snow flakes, dichroism may not be insignificant. One viable approach to determining the scattering parameters for nonspherical particles is the System Transfer Operator approach (or T-matrix method). By using the extended boundary condition method [14], [15] the scattered electromagnetic field relates to the incident field through the T-matrix. A particularly useful characteristic of the T-matrix is that it reduces exactly to Mie Theory for spherical particles.

3.1.1 Vector Spherical Wave Functions

The T-matrix approach requires expanding the incident and scattered fields into vector spherical wave functions [9], [12]. The scalar Helmholtz equation

$$(\nabla^2 + k^2)\psi = 0 \tag{3.1}$$

has the outgoing solution, in spherical coordinates,

$$\psi_{mn}(kr, \theta, \phi) = h_n(kr) P_n^m(\cos\theta) \mathrm{e}^{\mathrm{j}m\phi}, \quad n = 0, 1, 2, ..., \, m = \pm 1, ... \pm n \tag{3.2}$$

where h_n are the spherical Hankel functions of the first kind given in (A.3), and P_n^m are the associated Legendre functions from (A.4). In addition, the regular wave function, which is finite at $r = 0$, is

$$\mathrm{Rg}\psi_{mn}(kr, \theta, \phi) = j_n(kr) P_n^m(\cos\theta) \mathrm{e}^{\mathrm{j}m\phi}, \quad n = 0, 1, 2, ..., \, m = \pm 1, ... \pm n \tag{3.3}$$

where Rg denotes that h_n is replaced with the spherical Bessel function j_n from (A.1). Since the electric field in a linear, isotropic and homogeneous medium is divergence-free, i.e., $\nabla \cdot \mathbf{E}(\mathbf{r}) = 0$, then $\mathbf{E}(\mathbf{r})$ satisfies the vector Helmholtz equation

$$\nabla^2 \mathbf{E}(\mathbf{r}) + k^2 \mathbf{E}(\mathbf{r}) = 0. \tag{3.4}$$

The scalar spherical wave functions (3.2) and (3.3) extend to vector spherical wave solutions for (3.4). Two sets of transverse vector spherical wave functions that satisfy the stated requirements are

$$\begin{aligned} \mathbf{M}_{mn}(kr, \theta, \phi) &= \gamma_{mn} \nabla \times (\mathbf{r}\, \psi_{mn}(kr, \theta, \phi)) \\ &= \gamma_{mn} h_n(kr) \mathbf{C}_{mn}(\theta, \phi) \end{aligned} \tag{3.5}$$

and

$$\begin{aligned} \mathbf{N}_{mn}(kr, \theta, \phi) &= \frac{1}{k} \nabla \times \mathbf{M}_{mn}(kr, \theta, \phi) \\ &= \gamma_{mn} \left\{ \frac{n(n+1)}{kr} h_n(kr) \mathbf{P}_{mn}(\theta, \phi) + \frac{1}{kr} \frac{\mathrm{d}}{\mathrm{d}(kr)} \left(kr\, h_n(kr)\right) \mathbf{B}_{mn}(\theta, \phi) \right\}, \end{aligned} \tag{3.6}$$

with

$$\gamma_{mn} = \left[\frac{(2n+1)(n-m)!}{4\pi n(n+1)(n+m)!} \right]^{1/2}. \tag{3.7}$$

$\mathrm{Rg}\mathbf{M}_{mn}$ and $\mathrm{Rg}\mathbf{N}_{mn}$ complete the two sets of vector spherical wave functions, respectively. $\mathbf{B}_{mn}$, $\mathbf{C}_{mn}$ and $\mathbf{P}_{mn}$ are vector spherical wave harmonics:

$$\mathbf{B}_{mn} = r\nabla\left[P_n^m(\cos\theta)\mathrm{e}^{\mathrm{j}m\phi}\right], \tag{3.8}$$

$$\mathbf{C}_{mn} = \nabla\times\left[\mathbf{r}P_n^m(\cos\theta)\mathrm{e}^{\mathrm{j}m\phi}\right], \tag{3.9}$$

$$\mathbf{P}_{mn} = \hat{\mathbf{r}}P_n^m(\cos\theta)\mathrm{e}^{\mathrm{j}m\phi}. \tag{3.10}$$

In addition to the two sets of transverse vector spherical wave functions, there is another set of longitudinal vector spherical wave functions that satisfies the vector Helmholtz equation:

$$\begin{aligned}\mathbf{L}_{mn}(kr,\theta,\phi) &= \frac{\gamma'_{mn}}{k}\nabla\psi_{mn}(kr,\theta,\phi)\\ &= \gamma'_{mn}\left\{\frac{\mathrm{d}}{\mathrm{d}(kr)}h_n(kr)\mathbf{P}_{mn}(\theta,\phi)+\frac{1}{kr}h_n(kr)\mathbf{B}_{mn}(\theta,\phi)\right\},\end{aligned} \tag{3.11}$$

where

$$\gamma'_{mn} = \left[\frac{(2n+1)(n-m)!}{4\pi(n+m)!}\right]^{1/2}. \tag{3.12}$$

Again, $\mathrm{Rg}\mathbf{L}_{mn}$ completes the set of vector spherical wave functions.

Using the vector spherical wave functions and wave harmonics, the dyadic $\bar{\mathbf{I}}\mathrm{e}^{\mathrm{j}\mathbf{r}'\cdot\mathbf{r}}$ is

$$\begin{aligned}\bar{\mathbf{I}}\mathrm{e}^{\mathrm{j}\mathbf{r}'\cdot\mathbf{r}} = \sum_{n=0}^{\infty}\sum_{m=-n}^{n}(-1)^m\mathrm{j}^n\frac{2n+1}{n(n+1)}\Bigg\{&\frac{n(n+1)}{\mathrm{j}\gamma'_{mn}}\mathbf{P}_{-mn}(\theta',\phi')\otimes\mathrm{Rg}\mathbf{L}_{mn}(r'r,\theta,\phi)\\ &+\frac{1}{\gamma_{mn}}\mathbf{C}_{-mn}(\theta',\phi')\otimes\mathrm{Rg}\mathbf{M}_{mn}(r'r,\theta,\phi)\\ &+\frac{1}{\mathrm{j}\gamma_{mn}}\mathbf{B}_{-mn}(\theta',\phi')\otimes\mathrm{Rg}\mathbf{N}_{mn}(r'r,\theta,\phi)\Bigg\}.\end{aligned} \tag{3.13}$$

3.1.2 The T-matrix

Given a plane electromagnetic wave in the form

$$\mathbf{E}(\mathbf{r}) = \mathbf{E}_0 \mathrm{e}^{\mathrm{j}k\hat{\mathbf{r}}'\cdot\mathbf{r}}, \quad \mathbf{E}_0 \cdot \hat{\mathbf{r}}' = 0, \tag{3.14}$$

the wave expands into vector spherical wave functions by taking the dot product of $\mathbf{E_0}$ and $\bar{\mathbf{I}}e^{\mathrm{j}\mathbf{r}'\cdot\mathbf{r}}$. Thus the incident and scattered fields is, in terms of vector spherical wave functions,

$$\mathbf{E}^i(\mathbf{r}) = \sum_{n=1}^{\infty}\sum_{m=-n}^{n}\left[a_{mn}\mathrm{Rg}\mathbf{M_{mn}}(k_1\mathbf{r}) + b_{mn}\mathrm{Rg}\mathbf{N_{mn}}(k_1\mathbf{r})\right] \tag{3.15}$$

and

$$\mathbf{E}^s(\mathbf{r}) = \sum_{n=1}^{\infty}\sum_{m=-n}^{n}\left[p_{mn}\mathbf{M_{mn}}(k_1\mathbf{r}) + q_{mn}\mathbf{N_{mn}}(k_1\mathbf{r})\right], \quad r > r_{\odot}, \tag{3.16}$$

where $r_{\odot}$ is the radius of the smallest sphere centered at the scattering element's origin that circumscribes that element. The coefficients a_{mn} and b_{mn} are

$$a_{mn} = 4\pi(-1)^m \mathrm{j}^n d_n \mathbf{E}_0 \cdot \mathbf{C}^*_{mn}(\theta')\mathrm{e}^{-\mathrm{j}m\phi'}, \tag{3.17}$$

$$b_{mn} = 4\pi(-1)^m \mathrm{j}^{n-1} d_n \mathbf{E}_0 \cdot \mathbf{B}^*_{mn}(\theta')\mathrm{e}^{-\mathrm{j}m\phi'}, \tag{3.18}$$

where

$$d_n = \left[\frac{2n+1}{4\pi n(n+1)}\right]^{1/2}. \tag{3.19}$$

The relationship between the scattered-field expansion coefficients and the incident field expansion coefficients is the T-matrix, with elements

$$p_{mn} = \sum_{n'=1}^{\infty} \sum_{m'=-n'}^{n'} \left(T^{11}_{mnm'n'} a_{m'm'} + T^{12}_{mnm'n'} b_{m'm'} \right), \tag{3.20}$$

$$q_{mn} = \sum_{n'=1}^{\infty} \sum_{m'=-n'}^{n'} \left(T^{21}_{mnm'n'} a_{m'm'} + T^{22}_{mnm'n'} b_{m'm'} \right). \tag{3.21}$$

In matrix form, the relationship is

$$\begin{bmatrix} \mathbf{p} \\ \mathbf{q} \end{bmatrix} = \begin{bmatrix} \mathbf{T}^{11} & \mathbf{T}^{12} \\ \mathbf{T}^{21} & \mathbf{T}^{22} \end{bmatrix} \begin{bmatrix} \mathbf{a} \\ \mathbf{b} \end{bmatrix} \tag{3.22}$$

Given the derived relationship between the incident and scattered field expansions, the scattering dyadic (2.8) is, in terms of the T-matrix elements,

$$\begin{aligned} \bar{\mathbf{A}}(\hat{\mathbf{n}}^s, \hat{\mathbf{n}}^i) = & \frac{4\pi}{k_1} \sum_{nmn'm'} \mathrm{j}^{n'-n-1} (-1)^{m+m'} d_n d_{n'} \mathrm{e}^{\mathrm{j}(m\phi^s - m'\phi^i)} \\ & \times \left\{ \left[T^{11}_{mnm'n'} \mathbf{C}_{mn}(\theta^s) + \mathrm{j} T^{21}_{mnm'n'} \mathbf{B}_{mn}(\theta^s) \right] \otimes \mathbf{C}^*_{m'n'}(\theta^i) \right. \\ & \left. + \left[-\mathrm{j} T^{21}_{mnm'n'} \mathbf{C}_{mn}(\theta^s) + T^{22}_{mnm'n'} \mathbf{B}_{mn}(\theta^s) \right] \otimes \mathbf{B}^*_{m'n'}(\theta^i) \right\}. \end{aligned} \tag{3.23}$$

Since the scattering dyadic results in the amplitude scattering matrix, (2.10)–(2.13), the T-matrix can give solutions for the elements of the amplitude scattering matrix. Once the scattering matrix is calculated, the extinction and scattering matrices and cross sections can be easily calculated.

3.1.3 The Extended Boundary Condition Method

The extended boundary condition method, developed in [15] and later outlined in [9], [12] is a technique for computing the T-matrix for particles of simple shape, and applies to rotationally symmetric particles.

Just as the incident field expands into regular vector spherical wave functions, so does the field that is internal to the particle:

$$\mathbf{E}^{INT}(\mathbf{r}) = \sum_{n'=1}^{\infty} \sum_{m'=-n'}^{n'} \left[c_{m'n'} \mathrm{Rg}\mathbf{M}_{\mathbf{m'n'}}(k_2\mathbf{r}) + d_{m'n'} \mathrm{Rg}\mathbf{N}_{\mathbf{m'n'}}(k_2\mathbf{r}) \right], \tag{3.24}$$

where k_2 is the wavenumber of the interior of the scatter and $\mathbf{r}$ is only valid inside the particle. Given the condition that the tangential components of the electric and magnetic fields must be continuous across the boundary of the particle surface, the linear relation between the incident and internal fields is

$$\begin{bmatrix} \mathbf{a} \\ \mathbf{b} \end{bmatrix} = \begin{bmatrix} \mathbf{Q}^{11} & \mathbf{Q}^{12} \\ \mathbf{Q}^{21} & \mathbf{Q}^{22} \end{bmatrix} \begin{bmatrix} \mathbf{c} \\ \mathbf{d} \end{bmatrix}. \tag{3.25}$$

The elements of $\mathbf{Q}$ are

$$Q^{11}_{mnm'n'} = -\mathrm{j}k_1k_2J^{21}_{mnm'n'} - \mathrm{j}k_1^2J^{12}_{mnm'n'}, \tag{3.26}$$

$$Q^{12}_{mnm'n'} = -\mathrm{j}k_1k_2J^{11}_{mnm'n'} - \mathrm{j}k_1^2J^{22}_{mnm'n'}, \tag{3.27}$$

$$Q^{21}_{mnm'n'} = -\mathrm{j}k_1k_2J^{22}_{mnm'n'} - \mathrm{j}k_1^2J^{11}_{mnm'n'}, \tag{3.28}$$

$$Q^{22}_{mnm'n'} = -\mathrm{j}k_1k_2J^{12}_{mnm'n'} - \mathrm{j}k_1^2J^{21}_{mnm'n'}, \tag{3.29}$$

where

$$\begin{bmatrix} J^{11}_{mnm'n'} \\ J^{12}_{mnm'n'} \\ J^{21}_{mnm'n'} \\ J^{22}_{mnm'n'} \end{bmatrix} = (-1)^m \int_S dS\hat{\mathbf{n}} \cdot \begin{bmatrix} \mathrm{Rg}\mathbf{M}_{m'n'}(k_2 r,\theta,\phi) \times \mathbf{M}_{-mn}(k_1 r,\theta,\phi) \\ \mathrm{Rg}\mathbf{M}_{m'n'}(k_2 r,\theta,\phi) \times \mathbf{N}_{-mn}(k_1 r,\theta,\phi) \\ \mathrm{Rg}\mathbf{N}_{m'n'}(k_2 r,\theta,\phi) \times \mathbf{M}_{-mn}(k_1 r,\theta,\phi) \\ \mathrm{Rg}\mathbf{N}_{m'n'}(k_2 r,\theta,\phi) \times \mathbf{N}_{-mn}(k_1 r,\theta,\phi). \end{bmatrix} \tag{3.30}$$

Additionally, the scattered field relates to the internal field by

$$\begin{bmatrix} \mathbf{p} \\ \mathbf{q} \end{bmatrix} = -\mathrm{Rg} \begin{bmatrix} \mathbf{Q}^{11} & \mathbf{Q}^{12} \\ \mathbf{Q}^{21} & \mathbf{Q}^{22} \end{bmatrix} \begin{bmatrix} \mathbf{c} \\ \mathbf{d} \end{bmatrix}. \tag{3.31}$$

where $\mathrm{Rg}\mathbf{Q}$ changes $J^{kl}_{mnm'n'}$ to $\mathrm{Rg}J^{kl}_{mnm'n'}$ resulting in the change of the vector wave functions $\mathbf{M}_{-mn}(k_1 r,\theta,\phi)$ and $\mathbf{N}_{-mn}(k_1 r,\theta,\phi)$ to $\mathrm{Rg}\mathbf{M}_{-mn}(k_1 r,\theta,\phi)$ and $\mathrm{Rg}\mathbf{N}_{-mn}(k_1 r,\theta,\phi)$, respectively. Thus, the T-matrix, in terms of $\mathbf{Q}$, is

$$\mathbf{T} = -(\mathrm{Rg}\mathbf{Q})\mathbf{Q}^{-1} \tag{3.32}$$

While the solution for the T-matrix is in terms of single particle, it extends easily to collections of particles. The collections of particles represent a single scattering medium, as implied in Section 2.3.

3.2 Particle Orientation

The symmetries introduced by the orientations of particles within a medium greatly effect the scattering properties of that medium. If a large collection of particles

are randomly oriented, such that the distribution of orientation is uniform, then the medium is considered completely mirror symmetric and isotropic. Preferential alignment of particles removes some of the symmetries, and the medium is no longer isotropic. This section outlines the scattering properties derived from the T-matrix for various configurations of particle collections, along with the physical implications of these configurations. All particles considered are axisymmetric, e.g., spheres and spheroids. To help understand particle orientation, Section 3.2.1 gives brief descriptions of reference frames and rotation angles. Then, Section 3.2.2 explains randomly oriented particles, including the special case of spheres, and finally Section 3.2.3. discusses preferentially aligned particles.

3.2.1 Reference Frames

The frame-of-reference of a particle is the most convenient spatial configuration to use when calculating the scattering properties of that particle. This is especially true for axisymmetric, or rotationally symmetric, bodies such as spheroids, plates, and cylinders. Usually the rotational axis is aligned with the z-axis of the particle. Applications of scattering properties, such as remote sensing, may require that the observational reference frame differs from that of the particle. Selecting right-handed coordinate systems for both the observational and particle reference frames, a point

in observational space has coordinates $\{x_o, y_o, z_o\}$ while a point in particle space has coordinates $\{x_p, y_p, z_p\}$. Three Euler angles of rotation, α, β, γ, represent the transformation from observational coordinates to particle coordinates. α is the rotation of the observational coordinate system about the z_o-axis, where $0 \leq \alpha < 2\pi$, so that the new y-axis aligns with the intersections of the $x_o y_o$- and $x_p y_p$-planes. After rotating through the angle α, β is the rotation about the new y-axis, where $0 \leq \beta \leq \pi$. γ is the rotation about the z_p-axis, where $0 \leq \gamma < 2\pi$. While the wave incidence and scattering directions are defined in the observational reference frame, the previously defined methods assume particle space. To calculate the scattering properties in the observational reference frame, the incidence and scattering angles must first be transformed to the particle reference frame. Then, the scattering calculations are computed in particle space, before being transformed back to observational space.

3.2.2 Randomly-Oriented Axisymmetric Particles

By asserting that a collection of particles is randomly oriented, the assumption is made that the distribution of particle orientations is uniform and, thus, the medium as a whole is considered isotropic. Additionally, due to the randomness of the particle orientation, the medium is also considered mirror-symmetric about any plane. These assumptions greatly simplify calculations, particularly because the scattering proper-

ties of the medium are not dependent on the specific incidence or scattering direction, and instead are functions of the angle between the two directions. To illustrate this configuration, the plane that contains the incident and scattered waves defines the phase matrix, given that the incident beam is along the positive z direction of the particle, so that the matrix is solely a function of the scattering angle θ^s. This defines the scattering matrix:

$$\mathbf{F}(\theta^s) = \mathbf{Z}(\theta^s, \phi^s = 0, \theta^i = 0, \phi^i = 0). \tag{3.33}$$

Since the considered medium depends only on the difference between the incident and scattering directions, then θ^s is the angle Θ, where $\Theta = \arccos(\hat{\mathbf{n}}^i \cdot \hat{\mathbf{n}}^s)$. This results in a block diagonal matrix of the form

$$N \langle \mathbf{F}(\Theta) \rangle = \begin{bmatrix} F_{11}(\Theta) & F_{12}(\Theta) & 0 & 0 \\ F_{12}(\Theta) & F_{22}(\Theta) & 0 & 0 \\ 0 & 0 & F_{33}(\Theta) & F_{34}(\Theta) \\ 0 & 0 & -F_{34}(\Theta) & F_{44}(\Theta) \end{bmatrix}, \tag{3.34}$$

where $\langle \mathbf{F}(\Theta) \rangle$ is the ensemble-averaged scattering matrix for the medium. The ensemble-averaged scattering matrix is further simplified when scattering only along

the forward direction is considered:

$$N\left\langle \mathbf{F}(0)\right\rangle = \begin{bmatrix} F_{11}(0) & 0 & 0 & 0 \\ 0 & F_{22}(0) & 0 & 0 \\ 0 & 0 & F_{22}(0) & 0 \\ 0 & 0 & 0 & F_{44}(0) \end{bmatrix} \tag{3.35}$$

Since the particles are axisymmetric the elements of the forward scattering matrix must fit the constraints of $F_{44}(0) = 2F_{22}(0) - F_{11}(0)$ and $0 \leq F_{22}(0) \leq F_{11}(0)$. Along with the simplified forward scattering matrix, the extinction matrix is also diagonal:

$$\mathbf{K}(\hat{\mathbf{n}}) = N\left\langle C_{ext}\right\rangle \begin{bmatrix} 1 & 0 & 0 & 0 \\ 0 & 1 & 0 & 0 \\ 0 & 0 & 1 & 0 \\ 0 & 0 & 0 & 1 \end{bmatrix} \tag{3.36}$$

The backscattering case results, similarly, in diagonal matrices. Since the medium is effectively homogeneous, the emission is both isotropic and unpolarized, and is characterized by the absorption cross section $\langle C_{abs}\rangle$.

Integrating the phase matrix over the Euler rotation angles results in the ensemble-averaged scattering matrix:

$$\left\langle \mathbf{F}(\Theta)\right\rangle = \frac{1}{8\pi^2}\int_0^{2\pi} \mathrm{d}\alpha \int_0^{\pi} \mathrm{d}\beta \sin\beta \int_0^{2\pi} \mathrm{d}\gamma \mathbf{Z}(\theta^s = \Theta, \phi^s = 0, \theta^i = 0, \phi^i = 0, \alpha, \beta, \gamma). \tag{3.37}$$

The ensemble-averaged extinction and scattering cross sections derive directly from the elements of the T-matrix:

$$\langle C_{ext} \rangle = -\frac{2\pi}{k_1^2} \mathrm{Re} \sum_{n=1}^{\infty} \sum_{m=-n}^{n} \left[T_{mnmn}^{11} + T_{mnmn}^{22} \right], \tag{3.38}$$

$$\langle C_{sca} \rangle = -\frac{2\pi}{k_1^2} \sum_{n=1}^{\infty} \sum_{m=-n}^{n} \sum_{n'=1}^{\infty} \sum_{m'=-n'}^{n'} \sum_{k=1}^{2} \sum_{l=1}^{2} \left| T_{mnm'n'}^{kl} \right|. \tag{3.39}$$

From (3.38) and (3.39), (2.43) calculates the ensemble-averaged absorption cross section.

The diagonal properties of the extinction matrix and the forward scattering matrix, in addition to the unpolarized nature of the emission, show that there is no dichroism for forward propagating waves. The only polarizing effect is of photons that scatter into the direction of propagation from some other direction. The block-parallel structure of the scattering matrix ensures that the I and Q components of the Stokes vector remain independent of the U and V components.

The complete symmetry of spheres results in total independence with respect to orientation. Thus, the amplitude scattering matrix becomes diagonal, and the scattering

matrix simplifies even further from the more general randomly oriented particle case:

$$N\left\langle \mathbf{F}(\Theta)\right\rangle = \begin{bmatrix} F_{11}(\Theta) & F_{12}(\Theta) & 0 & 0 \\ F_{12}(\Theta) & F_{11}(\Theta) & 0 & 0 \\ 0 & 0 & F_{33}(\Theta) & F_{34}(\Theta) \\ 0 & 0 & -F_{34}(\Theta) & F_{33}(\Theta) \end{bmatrix}. \tag{3.40}$$

The T-matrix reduces to Mie theory for the case of the sphere.

3.2.3 Preferentially-Aligned Axisymmetric Particles

The preferential alignment of nonspherical particles has a considerable effect on the scattering properties of the medium as a whole. The medium is no longer isotropic nor is it symmetric about all planes; therefore, direction and polarization are key in understanding the scattering properties of aligned particles. In general, the entire amplitude scattering matrix is significant when dealing with preferentially aligned, arbitrary particles. The 4×4 identity matrix and the scalar extinction cross section do not compose the extinction matrix, which is no longer diagonal. The scattering matrix is not block-diagonal, and the phase matrix depends on both the incident and scattering directions. The full absorption vector must also be considered.

Simplifications can be made, however, when considering axisymmetric particles that are aligned with the observational reference frame. Examples of such a configurations

are falling hydrometeors, such as rain and snow, which are commonly modeled as oblate spheroids with the axis of symmetry aligned with the observational z-axis. Scattering is not dependent on the azimuthal component of the incidence direction. The amplitude scattering matrix becomes diagonal in the forward scattering direction, i.e., $\langle S_{12}(\hat{\mathbf{n}}, \hat{\mathbf{n}})\rangle = \langle S_{21}(\hat{\mathbf{n}}, \hat{\mathbf{n}})\rangle = 0$. This results in the extinction matrix consisting of only three independent elements:

$$\langle \mathbf{K}(\theta)\rangle = \begin{bmatrix} \langle K_{11}(\theta)\rangle & \langle K_{12}(\theta)\rangle & 0 & 0 \\ \langle K_{12}(\theta)\rangle & \langle K_{11}(\theta)\rangle & 0 & 0 \\ 0 & 0 & \langle K_{11}(\theta)\rangle & \langle K_{34}(\theta)\rangle \\ 0 & 0 & -\langle K_{34}(\theta)\rangle & \langle K_{11}(\theta)\rangle \end{bmatrix}, \tag{3.41}$$

where

$$\langle K_{11}(\theta)\rangle = \frac{2\pi}{k_1}\mathrm{Im}\left[\langle S_{11}(\hat{\mathbf{n}}, \hat{\mathbf{n}})\rangle + \langle S_{22}(\hat{\mathbf{n}}, \hat{\mathbf{n}})\rangle\right], \tag{3.42}$$

$$\langle K_{12}(\theta)\rangle = \frac{2\pi}{k_1}\mathrm{Im}\left[\langle S_{11}(\hat{\mathbf{n}}, \hat{\mathbf{n}})\rangle - \langle S_{22}(\hat{\mathbf{n}}, \hat{\mathbf{n}})\rangle\right], \tag{3.43}$$

$$\langle K_{34}(\theta)\rangle = \frac{2\pi}{k_1}\mathrm{Re}\left[\langle S_{22}(\hat{\mathbf{n}}, \hat{\mathbf{n}})\rangle - \langle S_{11}(\hat{\mathbf{n}}, \hat{\mathbf{n}})\rangle\right]. \tag{3.44}$$

In this case there is no forward scattered or backscattered dependence between I & Q and U & V. Additionally, there are no emission components for U and V [13]. For non-polarized incident radiation, or incident radiation with only linear (v and h) polarization, there are only third and fourth Stokes components generated when waves are scattered from incident directions that are not along the direction of propagation.

CHAPTER 4
SIMULATION COMPONENTS

The previous chapters have given a general explanation of the physics behind the interaction of electromagnetic wave with particles and groups of particles such as hydrometeors and other elements in an atmosphere. Now these theories must be combined to calculate the transfer of electromagnetic radiation through a specified atmosphere. This chapter details the tools used in assembling the radiative transfer model for simulating the Stokes vector in a precipitating atmosphere.

Section 4.1 explains the precipitation profiles used in the scattering calculations and how particle distributions are derived from this information. Section 4.2 gives the equations that govern the dielectric properties for liquid and ice particles. Finally, Section 4.3 details the tools used for radiative transfer calculations.

4.1 Precipitation Modeling

Understanding the effects of precipitation on microwave radiation requires a proper model of cloud microphysics. Knowledge of liquid and ice water profiles is necessary to generate particle size distributions and shapes for generating and scaling rain and ice (snow and graupel) scattering properties. The Goddard Cumulus Ensemble (GCE)

model [16] is a tool used to describe the complex environment of convective systems in four dimensions. GCE simulations have proven useful in providing the vertical cloud structure required for detailed radiative transfer calculations and retrieval inversions [3], [17]. Section 4.1.1 details the quantities used from the chosen GCE simulation for radiative transfer calculations, and Section 4.1.2 explains the statistical distribution that model the number of particles for given liquid and ice water densities.

4.1.1 Cloud Structure

Data from a GCE simulation of a tropical squall line that developed near the TOGA COARE observational array [18] in the western Pacific Ocean on 22 February 1993 provides liquid and ice profiles for radiative transfer calculations. The available simulation data file has a horizontal resolution of 2 km on a 140 by 140 pixel grid. The vertical profile consists of 28 layers, plus the surface. From the surface to an altitude of 10 km, each layers is resolved at 0.5 km, and above this altitude, layers are resolved at 1 km, to a bounding height of 18 km.

Since falling hydrometeors are the primary mechanism for scattering due to the large size (on the order of a few millimeters or more), especially at 37 GHz, these quantities are modeled carefully. Figs. 4.1 and 4.2 show the profiles of falling ice (graupel and snow) and rain, respectively. The simulations also include cloud ice and liquid,

since these also affect the simulated radiances; however, scattering and, therefore, polarization effects are negligible due to the small particle size (on the order of tens of microns). With frozen and liquid water densities, particle size distributions can then be calculated. Determining the dielectric properties of the particles and calculating gas absorption both require the temperature profile. Additionally, gas absorption calculations depends on the pressure and humidity profile.

4.1.2 Particle Size Distributions

Accurate calculations of particle absorption, scattering and emission require knowledge of both particle sizes and the distribution of those particle sizes. Marshall and Palmer [19] describe the distribution of raindrop sizes to be an inverse exponential distribution of the form

$$N(D) = N_0 \exp^{-\lambda D}, \tag{4.1}$$

where D is drop diameter, $N(D)$ is the number density over the range $D + dD$, N_0 is intercept parameter, and λ is the slope of the distribution. Marshall and Palmer find an intercept of 0.08 cm^{-4} to be consistent with observations, and the slope typically relates to rain rate via a power law fit. The inverse exponential distribution extends to both snow and graupel. The intercept values vary with rain type and geographical location. The intercepts used in these simulations fall within typical

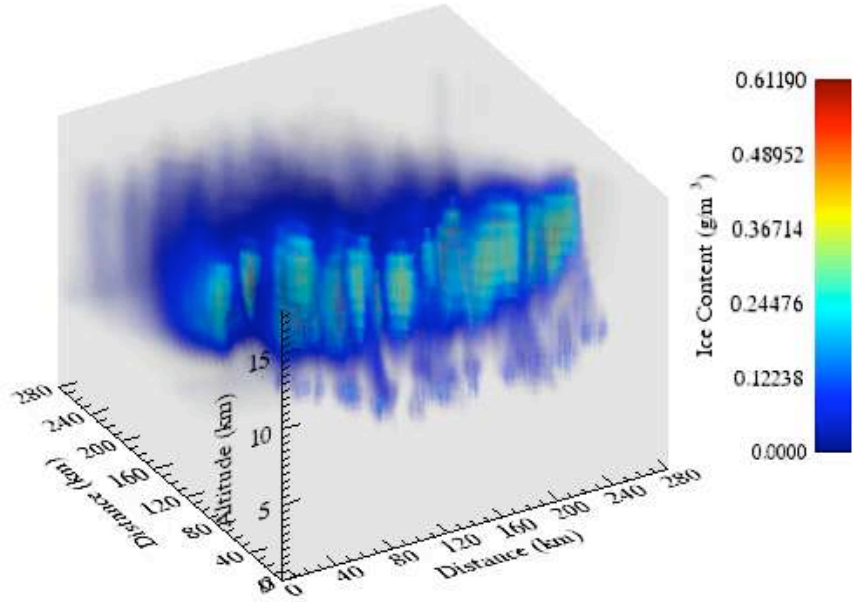

(a)

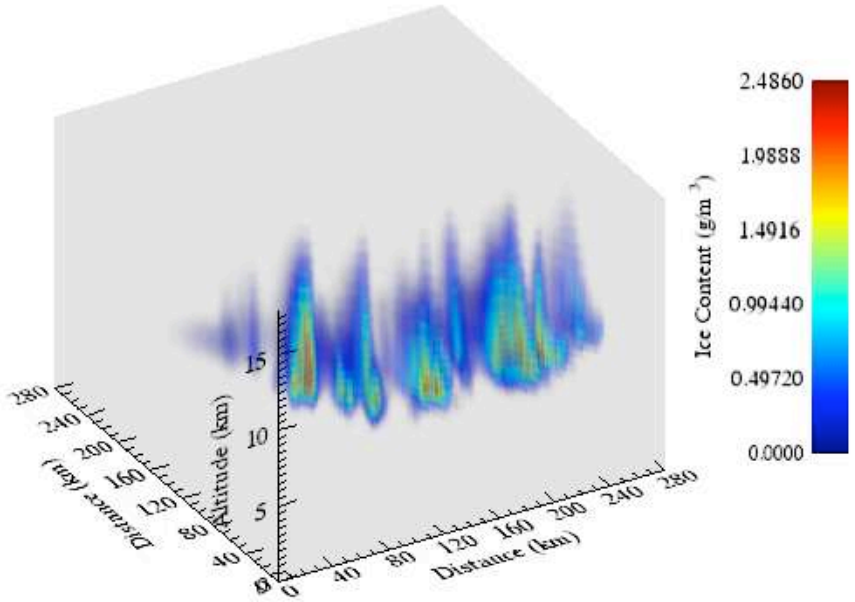

(b)

Figure 4.1: Precipitating ice profiles for snow (a) and graupel (b).

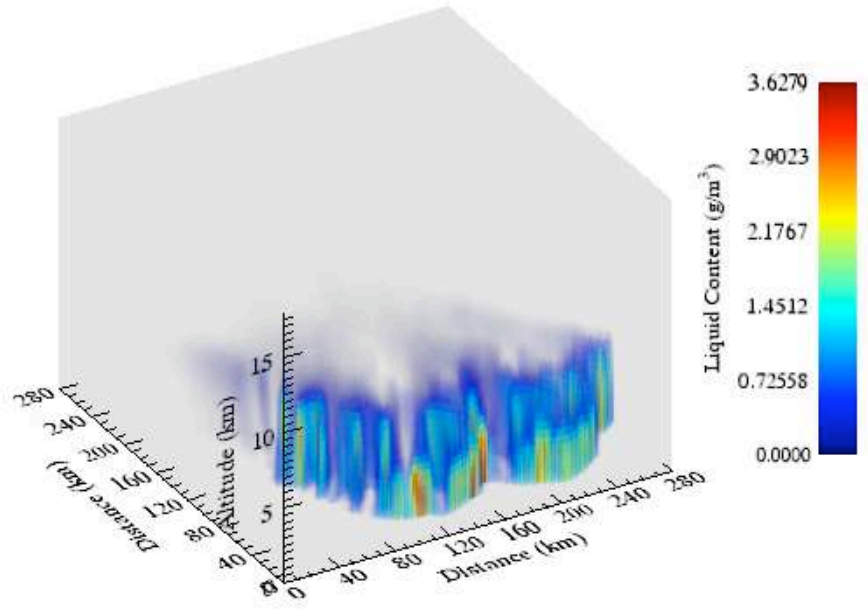

Figure 4.2: Precipitation profile for rain.

value ranges: rain and graupel is that of Marshall-Palmer, and snow is 0.17 cm^{-4}. Since water contents, not precipitation rates, are available from the GCE data set, λ must match the water content. To determine water content, the masses of the particles are integrated assuming spherical particles [20]:

$$C_W = \frac{1}{6}\int_0^\infty \rho N(D) D^3 \pi \mathrm{d}D, \tag{4.2}$$

where ρ is the particle density, 1 g/cm^3 for rain, 0.1 g/cm^3 for snow, and 0.4 g/cm^3 for graupel; and N(D) is the particle number distribution, in this case the inverse

exponential. By solving (4.2) and then inverting, λ equates to

$$\lambda = \left(\frac{N_0 \pi \rho}{C_W} \right)^{0.25}. \tag{4.3}$$

A modified gamma distribution represents the cloud liquid water distribution [21] and McFarquhar and Heymsfield [22] represents cloud ice.

4.1.3 Particle Shape

Besides particle size, particle shape is an important characteristic when considering the polarizing effects of hydrometeors. As rain falls, aerodynamical drag flattens the spherical shape of the drops, with the large dimension perpendicular to the drop direction. Snow crystals form as a hexagonal prism, from which dendritic arms grow. Snow particles "rock" back and forth as they fall, but the large dimension also tends to be perpendicular to the fall direction. At the frequencies of interest, the intricacies of the hydrometeor shapes are inconsequential; however, the general shape is of great importance. Standard practice is to estimate the shape of rain and snow as horizontally aligned oblate spheroids [23]. An oblate spheroid is an ellipse that is rotated about its minor axis. The oblateness of both rain and snow increase with the size of the hydrometeor. Oblateness, quantified by the aspect ratio, is the ratio of the major to minor axes of the defining ellipse. Since the distribution properties of precipitation

Table 4.1: Aspect Ratio Coefficients

c_0	1.0048
c_1	0.0057
c_2	2.628
c_3	3.682
c_4	1.677

depend on the volume of a sphere, as in (4.2), many polynomial expansions relate the aspect ratio to the radius (or diameter) of an equivalent volume sphere. The expansion chosen for this study is [24]

$$\frac{1}{R_A} = c_0 + \sum_{n=1}^{4} (-1)^{n-1} c_n D^n, \tag{4.4}$$

where Table 4.1 list the polynomial coefficients c_n.

Precision limitations place an upper bound to the aspect ratios of 2.5 and 3.4 for rain and snow, respectively. Since raindrops with radii larger than 4 mm become hydrodynamically unstable, the computational aspect ratio limit for rain results in physical significance, as an aspect ratio of 2.5 corresponds to a 4.9 mm drop radius.

Graupel forms when supercooled water droplets accrete on snow crystals and tends to be either spherical or conical. Graupel is assumed spherical for the purposes of these

simulations. Cloud droplets are also spherical, while the shape of cloud ice varies. Since cloud ice particles are much smaller than the smallest wavelength (about 20 microns versus 8 mm wavelength for 37 GHz), cloud ice is estimated as randomly oriented oblate spheroids with constant aspect ratio of 2.

4.2 Complex Refractive Index

In addition to particle size and shape, the absorption, emission and scattering quantities depend on the optical properties of hydrometeors. The complex refractive index gives information about how a medium slows the phase velocity of an electromagnetic wave in relation to a vacuum. For non-magnetic materials, such as water, the refractive index can be taken as the square root of the permittivity ϵ. The large imaginary component of the permittivity of liquid water at microwave frequencies over that of ice demonstrates the strongly absorptive properties of rain over that of snow or graupel, while both rain and snow/graupel have similar scattering cross sections. Still, computing the permittivity of rain is trivial when compared to snow or graupel as raindrops are considered pure liquid water. Graupel contains many air pockets within the ice structure. Although the small scale structure of snow is ignored for the scattering calculations, the spacing in the dendritic arms has an effect on the density and dielectric properties of the uniformly estimated particle. Thus, the spacings and

pockets are considered to be air inclusions when computing the dielectric properties of snow and graupel. Accurate T-matrix calculations require physically reasonable approximations of the dielectric properties of rain, snow and graupel. Most of the dielectric models are empirical fits of permittivity to frequency with a temperature dependence included.

[25] develops the frequency and temperature dependent dielectric properties for liquid water and pure ice. For liquid water, the double-Debye equation determines the permittivity.

$$\epsilon = (\epsilon_0 - \epsilon_1)\left[1 + \frac{f}{f_p}\right] + \frac{(\epsilon_1 - \epsilon_2)}{\left[1 + \mathrm{j}\frac{f}{f_s}\right]} + \epsilon_2 \tag{4.5}$$

where f is the frequency in GHz;

$$\epsilon_0 = 77.66 + 103.3(\theta - 1), \tag{4.6}$$

$$\epsilon_1 = 5.48, \tag{4.7}$$

and

$$\epsilon_2 = 3.51; \tag{4.8}$$

$$f_p = 20.09 - 142.4(\theta - 1) + 294(\theta - 1)^2, \tag{4.9}$$

and

$$f_s = 590 - 1500(\theta - 1). \tag{4.10}$$

$\theta = 300/T$ is the relative inverse temperature (Kelvin). For ice the permittivity is

$$\epsilon = 3.15 + \mathrm{j}(A/f + Bf), \tag{4.11}$$

where

$$A = [50.4 + 62(\theta - 1)]10^{-4}\mathrm{e}^{-22.1(\theta-1)}, \tag{4.12}$$

and

$$B = \frac{0.633}{\theta - 0.131} + \left[7.36 \times 10^{-4}\frac{\theta}{\theta - 0.9927}\right]^2. \tag{4.13}$$

For snow and graupel, the Maxwell-Garnett mixing scheme [26] introduces air inclusions and calculates an effective permittivity:

$$\epsilon_{MG} = \frac{1 - f_{air}\epsilon_{ice} + f_{air}\gamma\epsilon_{air}}{1 - f_{air} + f_{air}\gamma}, \tag{4.14}$$

where

$$\gamma = \frac{2\epsilon_{ice}Q}{\epsilon_{air} - \epsilon_{ice}}, \tag{4.15}$$

with

$$Q = \frac{\epsilon_{air}}{\epsilon_{air} - \epsilon_{ice}} \ln\left(\frac{\epsilon_{air}}{\epsilon_{ice}}\right) - 1. \tag{4.16}$$

f_{air} is the volume fraction of the air inclusions.

4.3 Atmospheric Radiative Transfer Simulator (ARTS)

ARTS is a flexible radiative transfer model capable of modeling diverse atmospheric conditions for a variety of sensor configurations and has been validated for frequen-

cies below 1 THz. The original implementation of ARTS (versions 1.0.xxx) is a one dimensional tool capable of generating atmospheric absorption coefficients for trace gasses such as water vapor, oxygen and nitrogen. It also calculates scalar radiative transfer. The more recent implementation of ARTS (versions 1.1.xxxx) extends radiative transfer calculations to up to three atmospheric dimensions and computes the full Stokes vector, which allows for the consideration of scattering [27]. ARTS is a collaborative effort, primarily between the University of Bremen, Bremen, Germany; and Chalmers University of Technology, Gothenburg, Sweden. The open source licensing for ARTS allows for free use and extension by outside scientists and developers. ARTS version 1.1.1095 (which shall be referred to as ARTS) is the primary tool used for this study. Since this version does not generate atmospheric absorption coefficients internally, ARTS version 1.0.195 (which shall be referred to as ARTS-1.0) generates these externally.

4.3.1 ARTS Gas Absorption

At 22.235 GHz, there is a weakly absorbing pressure-broadened spectral line due to changes in nuclear spin. There is a strong oxygen absorption band at 60 GHz resulting from changes in the orientation of electron spin with respect to molecular rotation. Of the frequencies of interest, gas absorption affects 10.7 GHz the least, with a small

contribution from water vapor and a negligible contribution from oxygen. 18.7-GHz simulations are sensitive to water vapor, and only slightly more sensitive to oxygen than those of 10.7-GHz. At 37 GHz there is an almost equal contribution of gas absorption from water vapor and oxygen; however, the total absorption is on par with that of 18.7 GHz [7]. Thus, water vapor and oxygen absorption must be considered when performing accurate atmospheric radiative transfer simulations. Also, nitrogen absorption is considered for completeness, even though contributions are minimal.

ARTS-1.0 is capable of computing absorption coefficients for both water vapor and oxygen using a number of popular models, including the Liebe Millimeter-wave Propagation model (MPM87, MPM89, and MPM93) [28]–[30] and the model of P.W. Rosenkranz (PWR98) [31], [32] which is a re-evaluation of the MPM series. This study utilizes the PWR98 model to generate gas absorption coefficients. To generate gas absorption coefficients, ARTS-1-0 requires the input of several geophysical parameters [33]. ARTS requires that separate absorption coefficients be derived for each of the three frequencies. These coefficients are calculated at varying pressures (altitudes) as a function of temperature and volume mixing ratio. Oxygen and nitrogen volume mixing ratios remain constant in the atmosphere. For water vapor, the mixing ratios are calculated pre-processing as follows. First, the saturation vapor

Table 4.2: Saturation Vapor Pressure Coefficients

a_0	6.107799961
a_1	$4.436518521 \times 10^{-1}$
a_2	$1.428945805 \times 10^{-2}$
a_3	$2.650648471 \times 10^{-4}$
a_4	$3.031240396 \times 10^{-6}$
a_5	$2.034080948 \times 10^{-8}$
a_6	$6.136820929 \times 10^{-11}$

pressure is calculated, based on empirical modeling by Flatau et al. [34]:

$$p_s = \sum_{n=0}^{6} a_n T^n, \tag{4.17}$$

where T is the temperature in Celsius. Table 4.2 details the polynomial coefficients a_n. The partial water vapor pressure $p_{\mathrm{H_2O}}$ is the product of the saturation vapor pressure and the relative humidity. The volume mixing ratio is then calculated at the ratio of the partial pressure of water vapor to that of dry air:

$$R_M = \frac{p_{\mathrm{H_2O}}}{p - p_{\mathrm{H_2O}}}, \tag{4.18}$$

where p is the air pressure.

Altitudes and the corresponding temperatures and volume mixing ratios are matched with air pressure and saved in text files for processing, and absorption coefficients are calculated for each pressure level, gas species, and frequency. Temperature perturbations may also be included so that absorption coefficients can be calculated at constant temperature offsets at each pressure level. This allows for interpolation of the absorption coefficients with respect to temperature when performing radiative transfer calculations within ARTS. After calculation, absorption coefficients, α, are converted to cross sections, α_{xsec}, to minimalize interpolation error [35]. This is done using the ideal gas law:

$$\alpha_{xsec} = \frac{\alpha}{nR_M}, \tag{4.19}$$

where the number of air molecules n is

$$n = \frac{p}{k_B T}. \tag{4.20}$$

p is air pressure in Pascals, k_B is Boltzmann's constant, and T is the temperature in Kelvin.

4.3.2 ARTS Scattering

Within ARTS, there are two available methods for performing radiative transfer calculations for scattering atmospheres: a discrete ordinate iterative (DOIT) method and a reversed Monte Carlo method [35]. The Monte Carlo method is used as it is

more suitable for three-dimensional radiative transfer calculations. While only one dimensional cases are simulated for this study, future research will demand the flexibility of including horizontal spatial variability of precipitation. The reverse Monte Carlo method [36] follows a prescribed number of photons from the measurement point backward through the scattering medium. The extinction contribution (including gas absorption) is calculated for a chosen propagation path length. By using a random number, a decision is made at the propagation path step of whether a photon is scattered or absorbed. If the photon is absorbed, the propagation path ends and the emission contribution is included. Otherwise, a new incident incident direction is chosen and the scattering contribution is logged. Once all photon tracing is complete, the contributions are combined, and the radiance at the measurement location is calculated, as well as the simulation error which gives a measure of accuracy or convergence. The accuracy of the simulation is controlled by the number of photons used in the scattering calculations; however, increasing the number of photons, and accuracy, increases runtime.

Scattering, emission, and absorption calculations are performed external to ARTS and are stored in extensible markup language (XML) files for use by the ARTS environment. Michael Mishchenko's FORTRAN T-matrix codes are utilized for scattering calculations. These codes have been modified and implemented in PyARTS [21]. PyARTS is a tool that allows for easy control of ARTS. It is capable of controlling

ARTS simulations, writing data files in XML for interaction with ARTS, and generating atmospheric data files and scattering parameters. Described below is how PyARTS uses Mishchenko's codes to create scattering data files.

To calculate the scattering data for snow and rain, the double-precision T-matrix code for nonspherical particles in fixed orientation [37] is used. First, the T-matrix is calculated once for a particle size and corresponding aspect ratio, incident wavelength, and complex index of refraction. Then the amplitude scattering matrix can be calculated for all incident and scattered directions. The extinction and phase matrices, as well as the absorption vector can easily be calculated directly from the amplitude scattering matrix using the equations from Sections 2.1.2 and 2.1.4. The extinction matrix is block diagonal, and the absorption vector only effects the I and Q components of the Stokes vector (see Section 3.2.3).

For graupel, cloud liquid, and cloud ice, the double-precision T-matrix code for nonspherical particles in random orientation [38] is used. The aspect ratios for graupel and cloud liquid are set at 1.000001 to avoid convergence issues of using an aspect ratio of exactly 1. Only one set of calculations is required, unlike the case of horizontally aligned particles. For a given particles size and corresponding aspect ratio, incident wavelength, and complex index of refraction, only the extinction and scatter-

ing cross section, and the block diagonal elements of the phase matrix are calculated as a function of scattering angle (see Section 3.2.2).

CHAPTER 5
SIMULATION METHODOLOGY

The polarization of radiation by precipitation offers both useful and destructive information. Since scattering, absorption and emission are related to particle properties such as size, shape, and hydrometeor phase, it is possible to determine cloud properties from polarization. Conversely, since precipitation offers such an overpowering signal, polarization effects from the hydrometeors can destructively interfere with the polarization information of the ocean surface needed to correctly retrieve wind direction. Since precipitation interferes with surface measurements three-fold–through absorption/emission, scattering, and augmentation of the ocean surface due to impacting drops–the complete electromagnetic interaction with both cloud structure and roughened ocean surface is complicated. Therefore, this dissertation only considers the effect of precipitation on polarization and ignores the polarizing effects of the ocean surface. Instead the sensitivities of the Stokes vector to wind direction can be used to make an indirect estimate of how precipitation in the atmosphere interferes with ocean surface retrievals.

Section 5.1 gives a short literature review of both passive microwave wind vector retrievals and simulations of microwave radiances in precipitation. This gives both perspective on the motivation behind this dissertation as well as an overview of some

similar research. Section 5.2 gives a detailed description of the two sets of simulations performed and the application of each simulation set to the analysis of how precipitation and instrument configuration affect the measured polarization.

5.1 Experiment Background

With respect to microwave remote sensing of the ocean, wave polarization is directly affected by two observables: wind vectors and precipitation. WindSat is proof-of-concept of the capability to retrieve the ocean surface wind vector through passive measurement of the full Stokes vector due to ocean surface emission and reflection [4]. For precipitation, both active [39] and passive [40] methods have been used to exploit the capabilities of polarization (primarily vertical and horizontal) to discriminate precipitation characteristics. Due to the large emission and scattering signatures of precipitation, ocean surface measurements are eclipsed by rain events that occur within instrument measurement fields-of-view. The aim of these simulations is to identify the precipitation signal present in microwave measurements by modeling the emission, absorption, and scattering signatures and performing radiative transfer calculations. A Lambertian surface with a constant emissivity is used for these simulations to avoid including complicated surface effects in the radiative transfer calculations, so that only the interference to precipitation is considered. However, a brief description

of passive ocean vector winds is given in Section 5.1.1 to emphasize the sensitivity of the polarimetric wind direction signal, and thus give motivation for the experiments performed for this dissertation. Section 5.1.2 details research efforts where simulations or theoretical calculations have been used to examine the polarization effects of precipitation.

5.1.1 Ocean Surface Emission and Reflection

Since the ocean surface is a boundary interface, a calm ocean with negligible wind speed results in specular reflection where the Fresnel reflection coefficients govern the reflection and emission. As wind flows over the fluid ocean surface, roughness of the boundary increases, which changes the reflection and emission characteristics; therefore, the Stokes vector increases with increasing roughness (wind speed). Also, the ocean surface roughness is preferential to wind direction. This results in separate harmonic dependences of the Stokes vector elements with respect relative wind direction, i.e., the difference between wind direction and viewing angle. The directional signal is highly sensitive to measurement errors and interference. The retrieval algorithm detailed in [6] gives the upper bounds of the co-polarization sensitivities of the brightness temperatures used for wind vector retrievals in the square root of the diagonal of the error covariance matrix S_y. The values for the wind speed range of

Table 5.1: Brightness temperature sensitivities in Kelvin for wind speeds 7-13 m/s.

	Frequency (GHz)		
	10.7	18.7	37.0
T_v	0.69	1.02	1.76
T_h	0.99	2.02	3.65
U	0.26	0.28	0.25
V	0.09	0.12	0.09

7-13 m/s for the frequencies and polarizations (modified Stokes) of interest are given in table Table 5.1.

5.1.2 Precipitation and Polarization

The research of polarization effects of precipitation in passive microwave radiometry has primarily focused on how Q is related to particle type and shape. Haferman [40] lists recent research efforts for both simulating and observing microwave radiances, specifically polarization, for precipitation. Haferman mentions a particular study by Roberti and Kummerow [41] that looks at simulations of cloud structure radiances for nonspherical hydrometeors, particularly the vertical and horizontal polarization.

While the study does not look directly at full Stokes vector, there are some useful insights and methods applicable to this dissertation.

Roberti and Kummerow perform Monte Carlo radiative transfer simulations for a set of one dimensional precipitation profiles for 19.35 GHZ, 37 GHz and 85.6 GHz at an incidence angle of 50°. Rain and snow are modeled as horizontally aligned oblate spheroids, while graupel is modeled as spheres. The aspect ratio of the rain is a function of drop size, while the aspect ratio of snow is uniform over all particle sizes. As part of the analysis, they increase the snow and reduce the graupel concentrations to determine the effects of nonspherical ice particles and to match observations. Results show polarization ($V - H$ or Q) differences up to 15 Kelvin, depending on frequency, but state that third Stokes values are small, and are only included for calculations, not analysis. Also, a conversion of 50% of the graupel to snow gives simulated results that match observation.

The literature on the effects of precipitation on the third Stokes parameter is sparse. One group of scientists from Germany and Russia have published a set of articles on the subject. The most relevant to this research is Kutuza et al. [42]. While the study is limited in scope, model calculations assert an appreciable third Stokes parameter in precipitation. The simulations include a canting angle (equivalent to a non-zero Euler angle β) which accounts for the horizontal drag component, i.e., horizontal wind in

the rain volume. This results in a non-zero emission component for the third Stokes parameter. However, the simulations only uses a uniform vertical profile and are only performed at nadir for upwelling simulations and zenith for downwelling simulations. Other simplifying assumptions are made, such that scattering by rain is ignored while emission and backscattering by ice is ignored. Results show U values on the order of 0.9 Kelvin of upwelling radiation at 35 GHz and 0.1 Kelvin at 13.3 and 20 GHz.

While both [41] and [42] claim that third Stokes values of upwelling radiation are small quantities, the values from Kutuza et al. when compared with the sensitivities in Table 5.1, show that small small contributions in the third Stokes can interfere with ocean vector wind retrievals.

5.2 Simulation Description

To determine the dichroism and thus interference due to precipitation, the calculations performed for this research simulate various combinations of precipitation scenarios and instrument properties. Ensemble-average scattering parameters are generated once for each of the frequencies of interest and are then stored to be loaded into ARTS for radiative transfer calculations, where they are scaled by the particle number densities. Simulations are conducted at WindSat frequencies at which fully polarized measurements are taken: 10.7 GHz, 18.7 GHz, and 37 GHz. Scattering will not have

much effect at 10.7 GHz and should have a small effect at 18.7 GHz, while both emission and scattering effects influence 37 GHz radiances [7].

To generate particle number densities, two separate sets of simulations have been formulated. The first set of data uses profiles from the GCE simulation detailed in Section 4.1.1 along a line perpendicular to the line of convection [41] to analyze the effects of liquid and ice content on polarization and frequency, and is referred to as "simulation set 1". To reduce the total number of profiles processed, and thus, processing time, a second set involving 12 GCE profiles of differing vertical structure is used to investigate the polarization effects with respect to incidence angle. This is referred to as "simulation set 2".

5.2.1 Simulation Set 1

The images presented in Fig. 5.1 are slices of the precipitation profiles given in Figs. 4.1 and 4.2 that are used for simulation set 1. Looking at the three dimensional profiles in Figs. 4.1 and 4.2, the slices are taken at the 158-km mark with respect to the axis "parallel" to the page and extend from the 32-km mark to the 152-km mark going into the page. Each vertical profile is considered an individual one dimensional profile. The slice of profiles gives a line of spatially correlated cloud structures that vary slowly with position. This collection of precipitation data allows for a close

inspection of the effect of a large number of combinations of rain, snow and graupel. All simulations for set 1 are calculated for an incidence angle of 50°.

5.2.2 Simulation Set 2

Plots of the precipitation profiles used for the second set of simulations are given in Figs. 5.2, 5.3, and 5.4. The plots are ordered by the maximum water content of any one precipitation phase (rain, snow or graupel) from least to greatest. The profiles are non-contiguous sub-clouds from the simulated cloud structure, and were chosen to represent a diverse set of rain, snow and graupel combinations, mostly in lighter precipitation conditions. The lighter water contents result in lower Monte Carlo simulation uncertainties. To examine if there is a relationship between polarization and the viewing incidence angle, radiances are calculated at incidence angles of 40°, 45°, 50°, 55° and 60° at each of the frequencies. The simulated incidence angles encompass the range of WindSat incidence angles of between 49° and 56°.

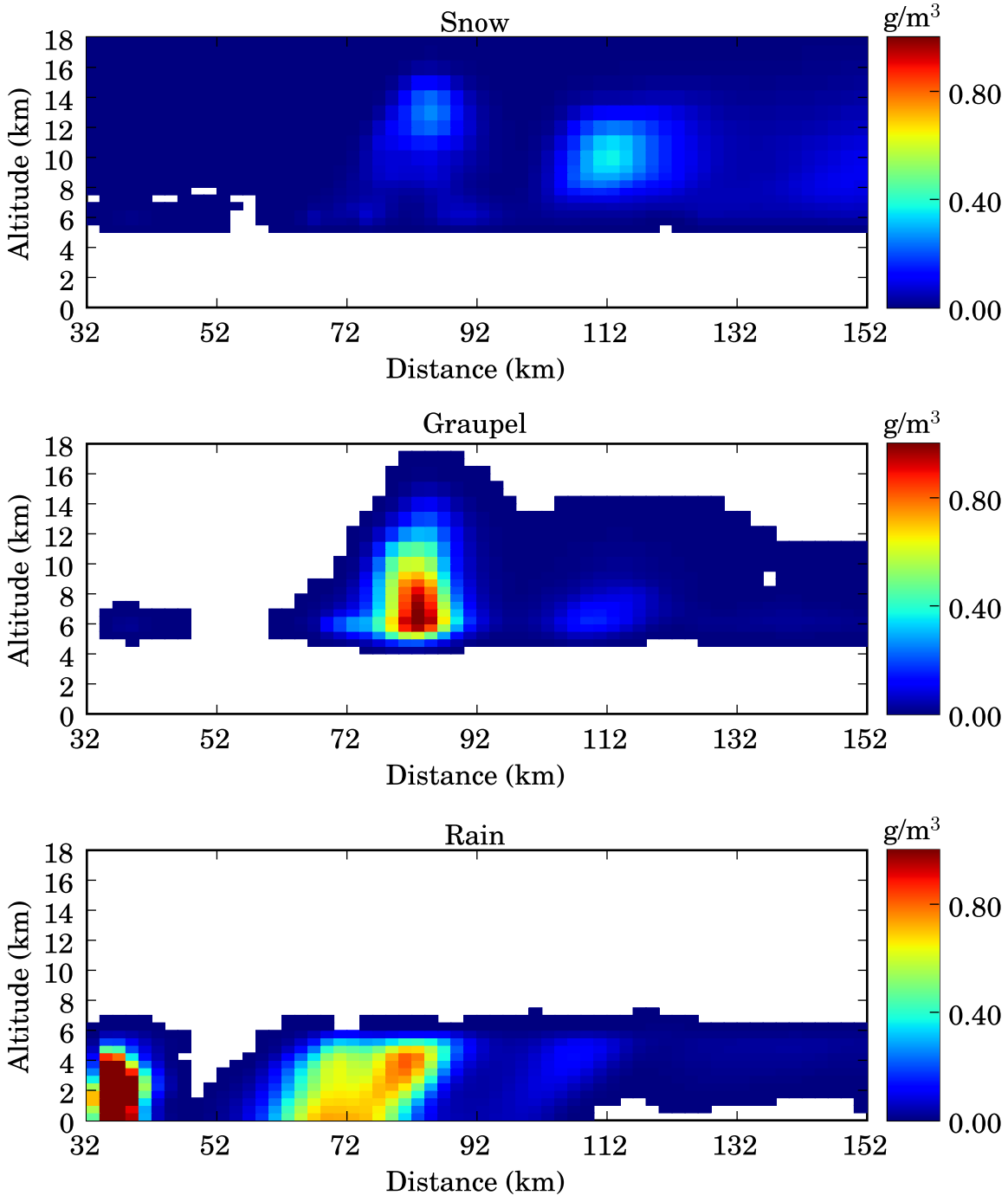

Figure 5.1: Images of the slices of precipitation profiles used for simulation set 1.

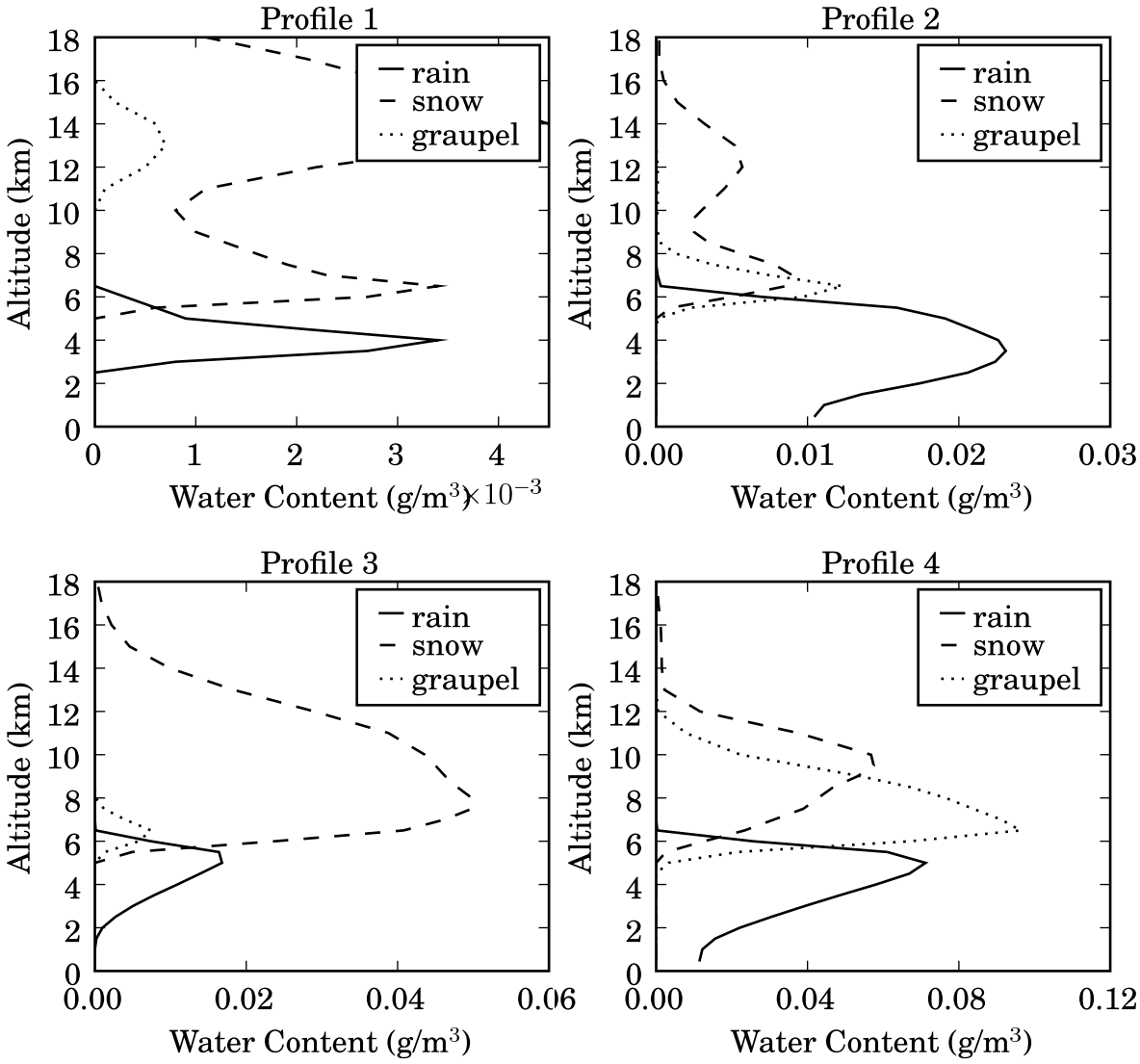

Figure 5.2: Profiles 1-4 for simulation set 2.

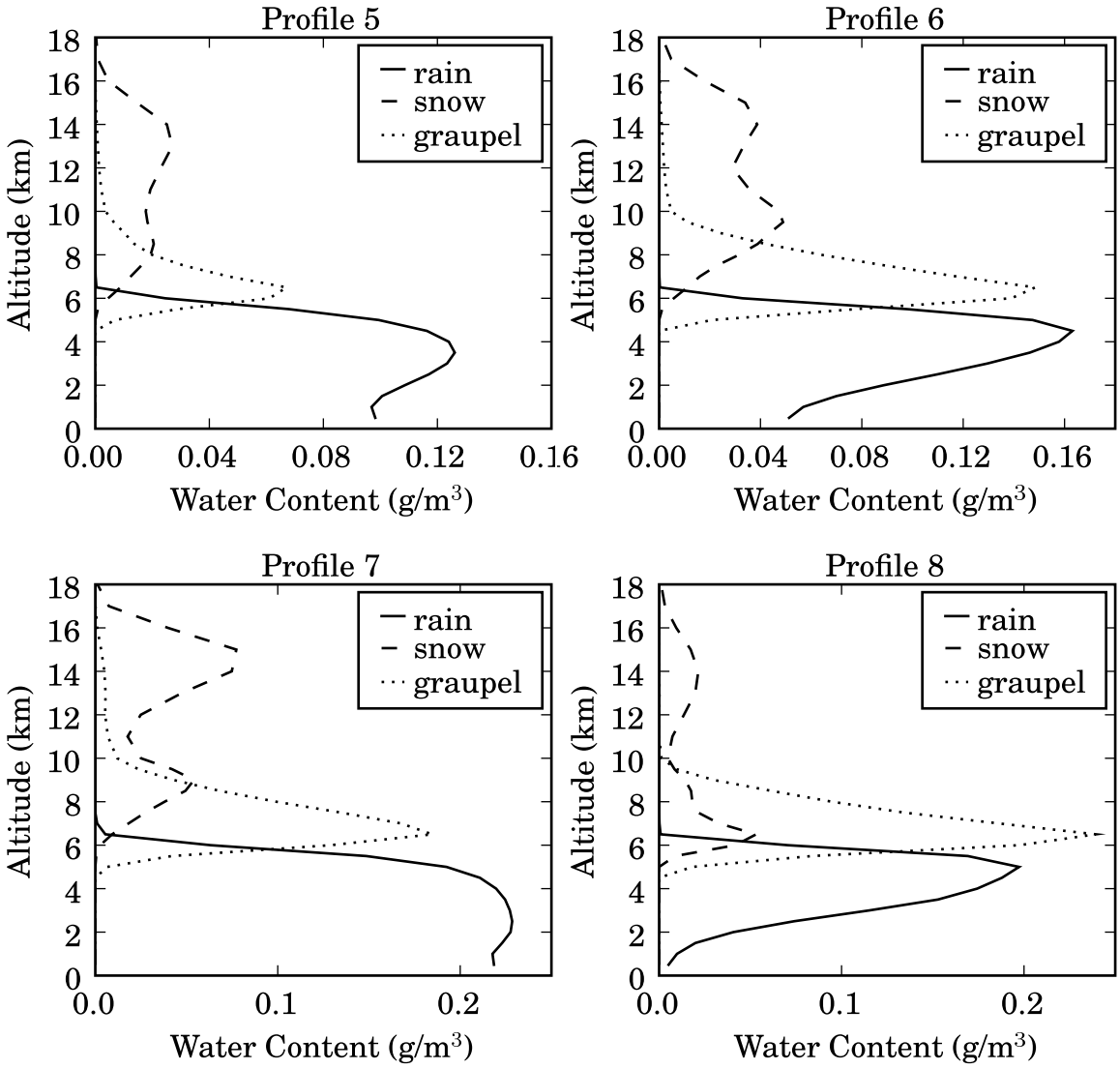

Figure 5.3: Profiles 5-8 for simulation set 2.

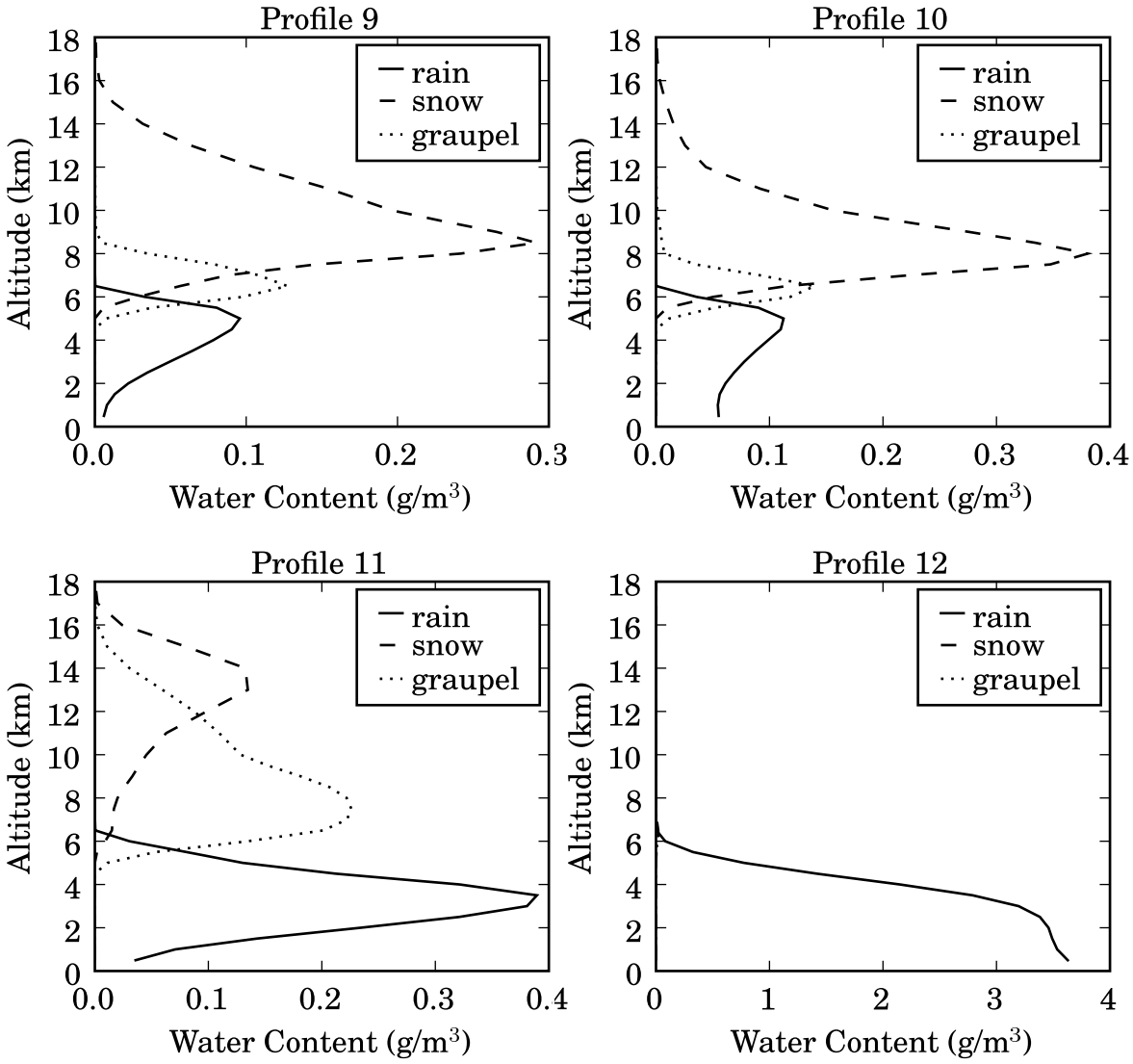

Figure 5.4: Profiles 9-12 for simulation set 2.

CHAPTER 6
RESULTS AND CONCLUSIONS

6.1 Accuracy Versus Runtime

Since a Monte Carlo simulation requires averaging a large number of independent trials, increasing accuracy requires extending the runtime due to the increased number of trials. In the case of Monte Carlo radiative transfer models, each trial follows an individual photon through its propagation path. This section presents a trade study between the number of photons required to reduce simulation noise below the accuracy of the desired signal and the runtime required for simulating the prescribed number of photons. All ARTS calculations take place on a dual-processor 1.8 GHz PowerMac G5, where the each processor calculates the contribution of half of the total number of photons.

Fig. 6.1 is the Monte Carlo simulation error for six independent simulations for a single profile from simulation set 1. The profile at distance 82 km, Fig. 5.1, consists of large amounts of rain, snow and graupel; therefore, it gives an upper bound to the Monte Carlo simulation uncertainty for the profiles used in this dissertation. Starting at 25,000 photons, each run doubles the amount of the photons from the previous run. The errors for I are about 1.5 times those of Q and 3 times those of U. Nominally,

the magnitude of I is on the order of 150 K to 290 K, whereas Q is usually a few Kelvin.

Fig. 6.2 gives the magnitude of the Stokes parameters simulated in the trade study. To emphasize the fluctuations in I, the mean for each frequency has been subtracted from the first Stokes brightness temperatures. The fluctuations for each of the Stokes parameters dampen with increased photons. While the magnitudes of both I and Q show appreciable signals, the magnitude of U converges toward 0 with increasing numbers of photons. Since this profile contains a large number of nonspherical particles, the lack of a discernible signal suggests that off angle scattering does not result in a measurable third Stokes signal. An equivalent analysis for distance marker 68 km shows similar results for the third Stokes parameter.

The simulation runtime plot, Fig. 6.3, shows that below about 100,000 photons, increasing the number of photons does not greatly increase runtime. Once the number of photons exceeds about 200,000, runtime increases drastically, making processing of large datasets cost(time)-prohibitive. Since fluctuations in Q minimize after about 100,000 photons, simulations in both sets 1 and 2 use 120,000 photons.

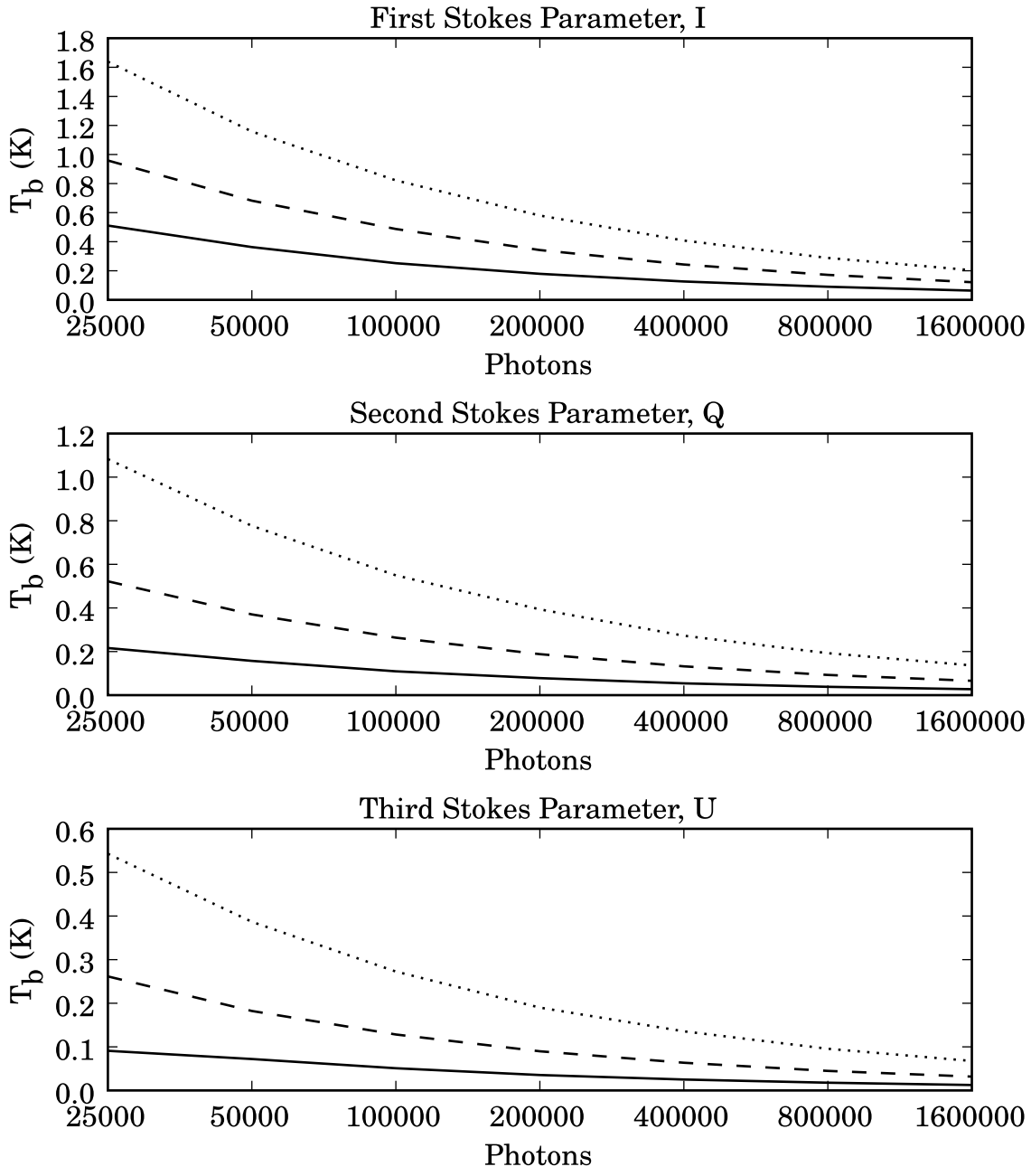

Figure 6.1: Stokes error vs. number of photons. Solid line is 10.7 GHz, dashed line is 18.7 GHz and dotted line is 37.0 GHz.

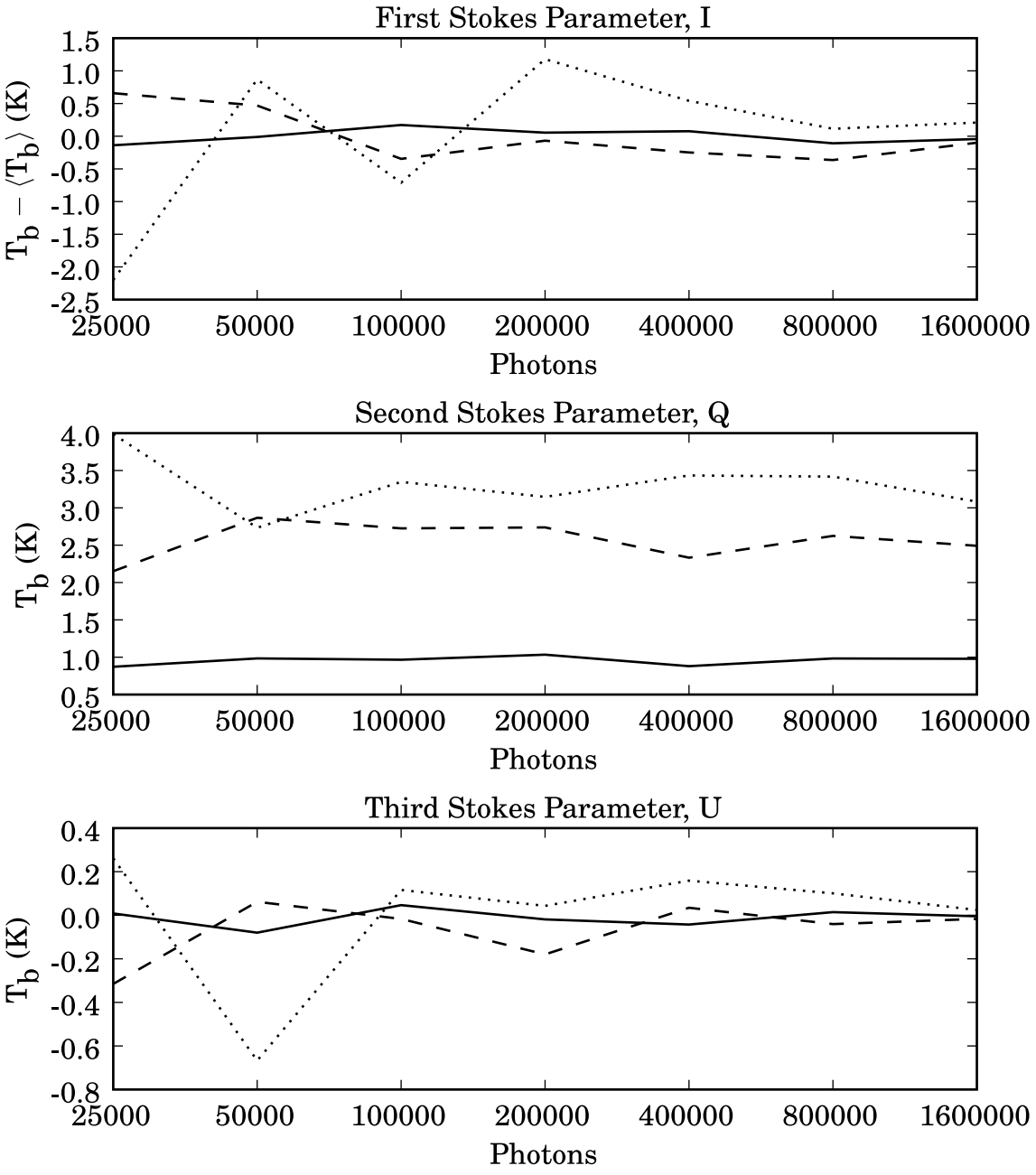

Figure 6.2: Stokes magnitude vs. number of photons. Solid line is 10.7 GHz, dashed line is 18.7 GHz and dotted line is 37.0 GHz. Since the magnitude of I tends to be much larger than fluctuations, the mean of I has been subtracted for each frequency.

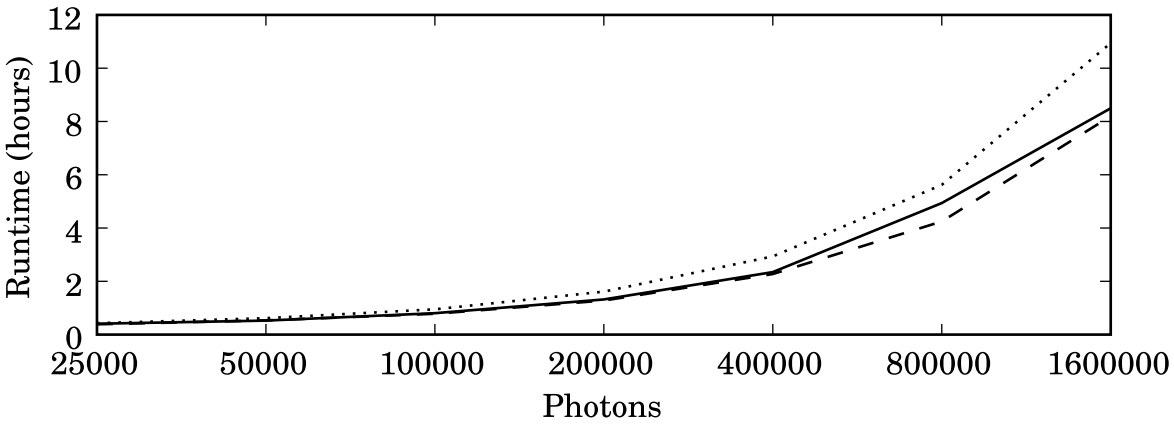

Figure 6.3: Monte Carlo runtime vs. number of photons. Solid line is 10.7 GHz, dashed line is 18.7 GHz and dotted line is 37.0 GHz.

6.2 Simulation Set 1 Results

The results for simulation set 1 show a definite frequency dependence in the effect that absorption, emission, and scattering have on polarization. The lack of a polarization signature in the third Stokes, as evident in the accuracy analysis, appears as noise in both simulation sets, since the large number of photons required to converge to 0 is cost-prohibitive. Q, however, shows a large polarization signal, both from scattering and from absorption/emission. The surface temperature of 300 Kelvin and an emissivity of 0.9 result in a high background brightness temperature; therefore, scattering and absorption will be the mechanisms apparent when examining I.

For 10.7 GHz, Fig. 6.4, the polarization signal is purely from emission and absorption. The largest changes in I and Q correspond to the profiles with the greatest amounts of rain in the 32-40 km range, while the snow and graupel between 76 and 88 km do not seem to add any contribution beyond that of rain. U appears as random noise with large errors in regions of high precipitation.

At 18.7 GHz, given in Fig. 6.5, absorption and emission are still the dominant mechanism; however, the effects of scattering are also noticeable. Unlike 10.7 GHz, the polarization effects in the regions with high snow and graupel is of similar magnitude to the region with large amounts of rain and negligible snow or graupel. Absorption effects are still the strongest mechanism, however. Also, from about 100 to 112 km the snow is polarizing the simulated radiation. Again, U appears as random noise.

Fig. 6.6 presents the simulation set 1 results for 37 GHz, which is much more sensitive to scattering. This is effect is quite apparent in I. The greatest dip in brightness temperature occurs where there is a large amount of snow and graupel. While rain absorption also results in lower intensities, the negligible absorption cross section and large scattering cross section of frozen water guarantee lower intensities.

Q, which gives the normalized difference between vertical and horizontal, shows an opposing signature to that of I. At first glance, increases in water content correspond directly to increased Q; however, the profile at and around the 82 km distance show

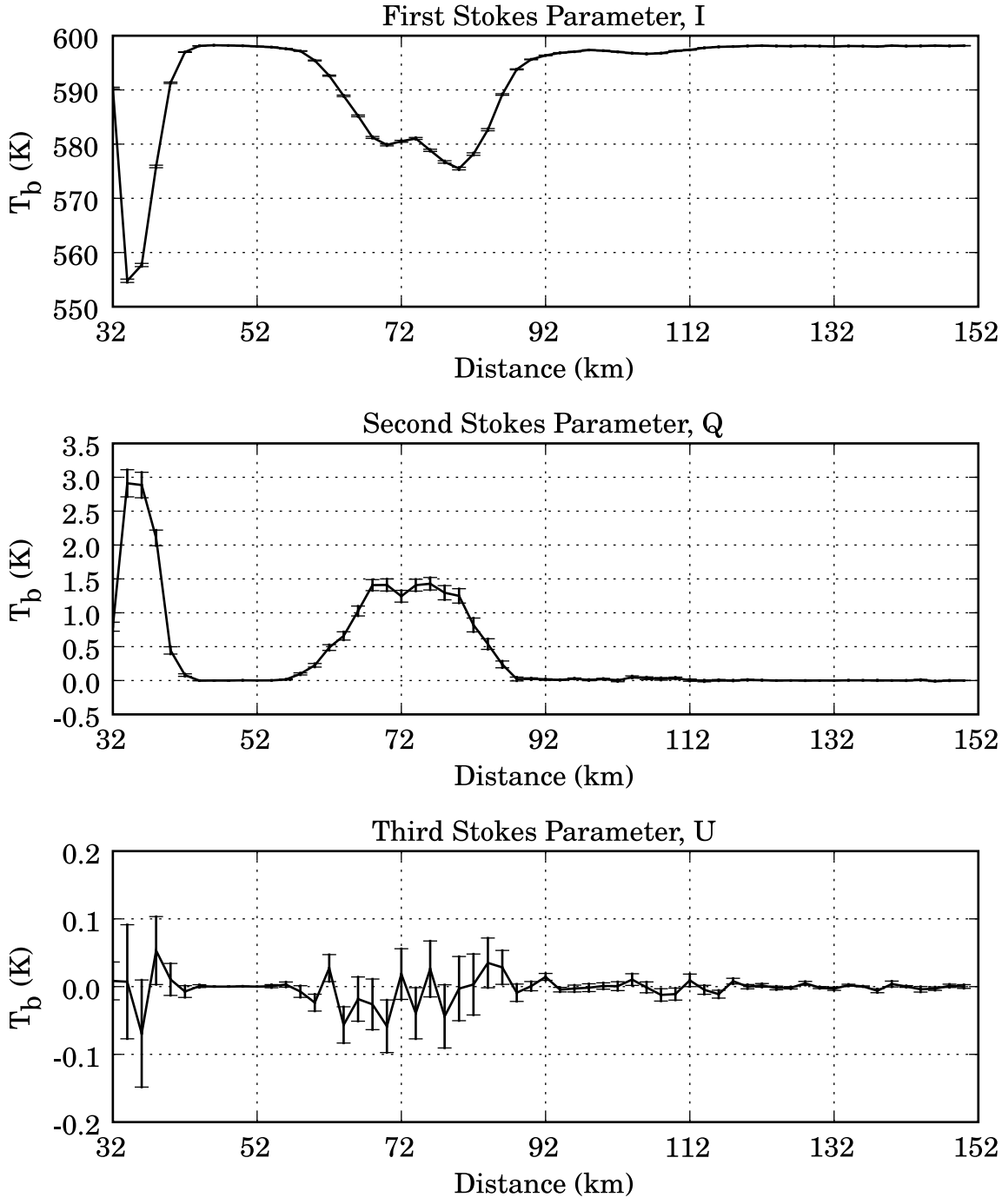

Figure 6.4: Simulation set 1 radiances for 10.7 GHz.

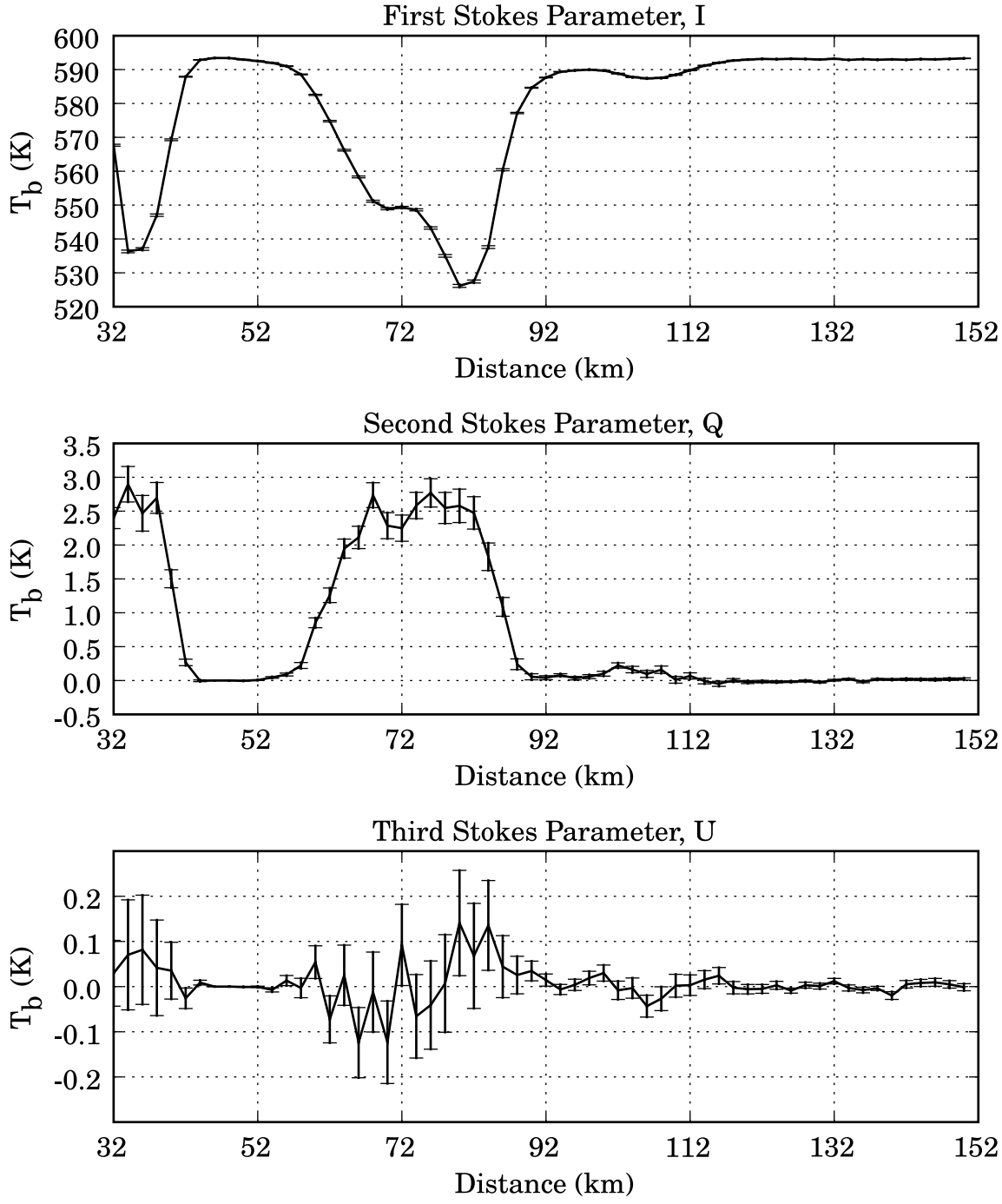

Figure 6.5: Simulation set 1 radiances for 18.7 GHz.

that the large graupel content results in a lower Q than for some of the neighboring profiles. Absorption also affects the polarization, as apparent in the region between 32 and 40 km. Scattering, however, is the strongest source of polarization, since the regions with high snow and graupel content result in the greatest dichroism.

Since the accuracy calculations show that the simulated third Stokes magnitudes seem to result from uncertainties in the radiative transfer model, scattering from directions off of the incident direction are negligible. As increased numbers of photons with off-angle contributions are considered, these effects average and slowly converge towards zero. Since the number of photons required to show this is cost-prohibitive, multiple independent runs of simulation set 1, Fig. B.1 and the bottom pane of Fig. 6.6, show that the third Stokes signal is random, with poor convergence at high water contents.

6.3 Simulation Set 2 Results

The entire listing of results for simulation set 2 is available in Appendix C in table format. Each table gives the results for one incidence angle at a particular frequency. Tables C.1 - C.5 give the Stokes vectors at 10.7 GHz. The only profile that results in a considerable polarization signal is 12, which consists of a large amount of rain. This is consistent with effect of emission at 10.7 GHz and the immunity of the channel to

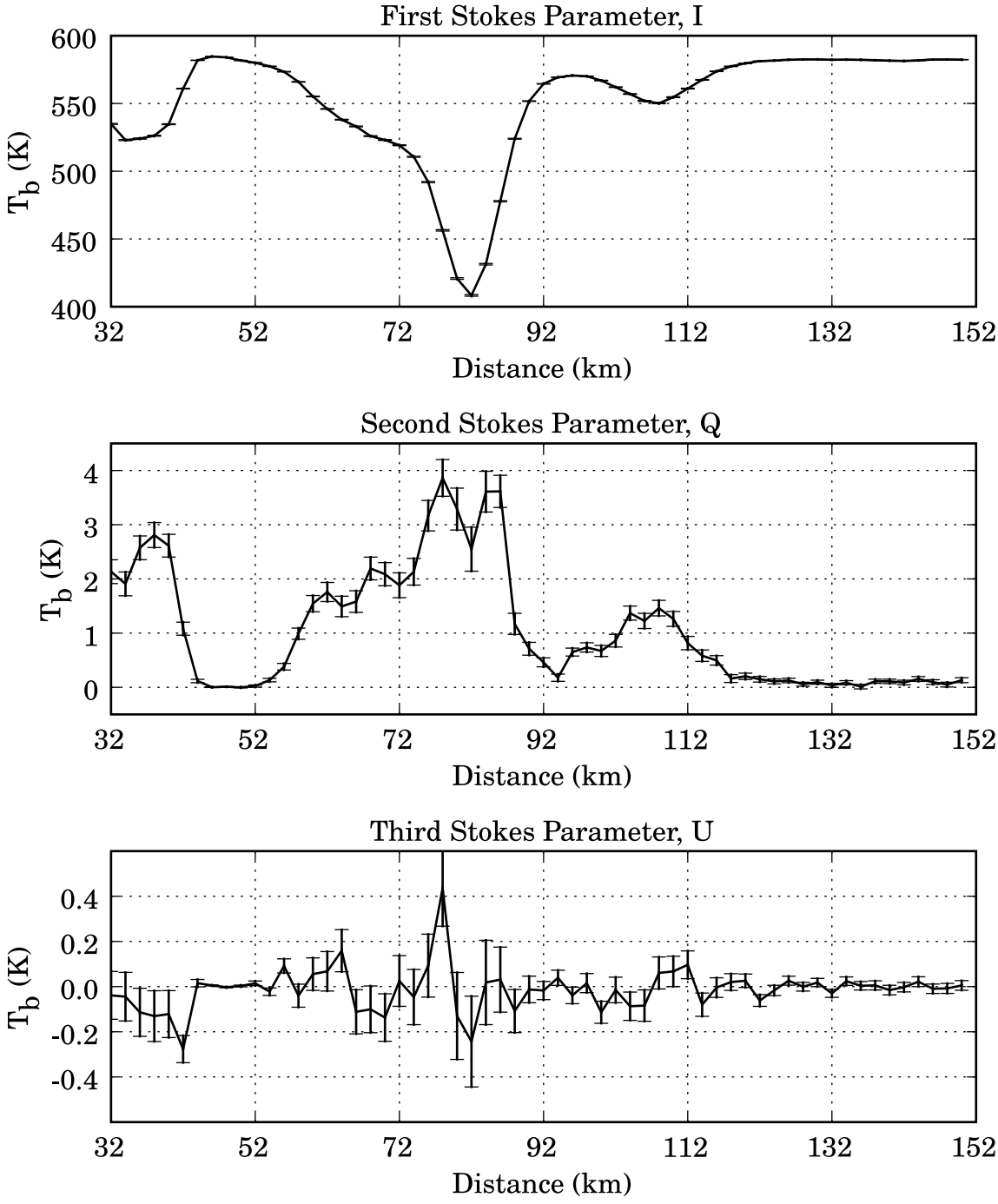

Figure 6.6: Simulation set 1 radiances for 37 GHz.

scattering. The polarization signal for all the other profiles is on the order of the noise for the simulations. Even looking only at profile 12, there is still a definite increase in polarization with respect to incidence angle.

Tables C.6 - C.10 present the polarized brightness temperatures at 18.7 GHz. Here profiles 6, 7, 8, 11, and 12 all show polarization effects, due to the combination of emission and a small scattering effect. The radiances for these profiles all increase with increasing incidence angle. As with 10.7 GHz, the largest polarization effect is due to emission.

Tables C.11 - C.15 give the brightness temperatures for 37.0 GHz. All of the profiles except 1, 2, and 3 all show at least a small but measurable polarization effect. Unlike 10.7 or 18.7, emission is no longer the dominant polarizer. Here profile 7 results in the largest Q. While rain is still the dominant precipitation phase, the appreciable level snow contributes to the polarization signal. As with the third Stokes results from simulation set 1, there is no useful information in U.

6.4 Conclusion

The results from both sets of simulations show a large atmospheric contribution in Q due to precipitation. The effects of hydrometeor phase are largely dependent on

frequency, since scattering effects are prominent when the size of the particle is on the order of the incident wavelength. In both the scattering and absorption cases, the polarization effect results from a greater extinction for the horizontally oriented electric field, since it has the same orientation as the large dimension of horizontally aligned oblate hydrometeors. At 37 GHz, where scattering is significant, a large amount of spherical graupel can result in a depolarization of effects introduced by the nonspherical hydrometeors. For all frequencies, the atmospheric Q from precipitation, when compared with the retrieval sensitivities in Table 5.1, will result in erroneous wind vector solutions. This is aggravated by the high incidence angles required by conical scanning sensors, like WindSat, to give adequate Earth coverage.

Unlike Q, the results show that there is no atmospheric signal for U. While the simulations ignore canting angle from horizontal wind in the atmosphere, the off-angle scattering is negligible. The accuracy analysis shows that when a large number of photons (1.6 million) are used, an appropriate distribution of photons scattered from direction not along the simulation line-of-sight are averaged to give an overall zero contribution. The lack of an atmospheric contribution does not mean that third Stokes measurements are completely immune to rain. Attenuation still effects the U component of surface emission and reflection, and precipitation impacting the surface will alter the surface structure itself. Also, by looking at the results from Q at 37 GHz, the depolarization may effect surface contributions of U. To investigate all of

the effects of precipitation on the surface signal, future research requires the inclusion of both a hydrometeor canting angle and a surface wind model. Regardless, there is still useful surface information at 10.7 GHz even at high rain rates, with some surface information present at lower rain rates at 18.7 GHz.

APPENDIX A
SPECIAL FUNCTIONS

The real-valued spherical Bessel functions of the first kind are

$$j_n(x) = x^n \left(-\frac{1}{x}\frac{\mathrm{d}}{\mathrm{d}x} \right)^n \left(\frac{\sin x}{x} \right). \tag{A.1}$$

The real-valued spherical Bessel functions of the second kind are

$$y_n(x) = -x^n \left(-\frac{1}{x}\frac{\mathrm{d}}{\mathrm{d}x} \right)^n \left(\frac{\cos x}{x} \right). \tag{A.2}$$

The Hankel functions of the first kind are a complex combination of the spherical Bessel functions:

$$h_n(x) = j_n(x) - \mathrm{j}y_n(x). \tag{A.3}$$

The associated Legendre functions are

$$P_l^m(x) = (-1)^m (1-x^2)^{m/2} \frac{\mathrm{d}^m}{\mathrm{d}x^m} P_l(x), \tag{A.4}$$

where $P_l(x)$ are the Legendre polynomials, given by

$$P_l(x) = \frac{1}{2^l l!}\frac{\mathrm{d}^l}{\mathrm{d}x^l}(x^2-1)^l. \tag{A.5}$$

APPENDIX B
INDEPENDENT THIRD STOKES SIMULATIONS

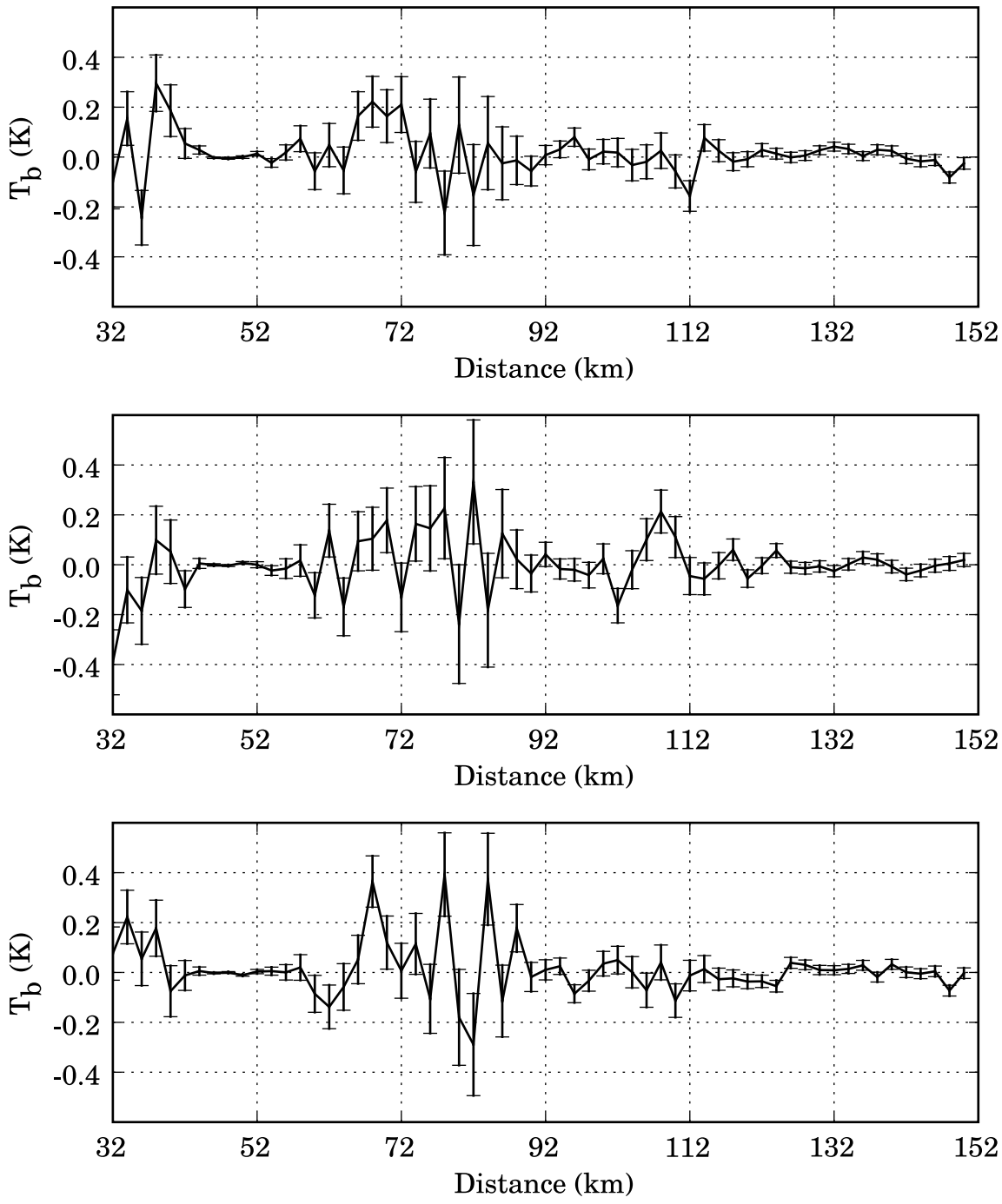

Figure B.1: Independent 37 GHz third Stokes simulations.

APPENDIX C
SIMULATION SET 2 OUTPUT TABLES

Table C.1: Brightness temperatures for 10.7 GHz at 40° incidence.

	I		Q		U	
Profile	T_b	$Error$	T_b	$Error$	T_b	$Error$
1	598.46	0.028	6.68e-07	4.09e-06	0	0
2	598.3	0.0292	0.00122	0.00339	0.000852	0.00189
3	598.35	0.0298	0.000211	0.000156	-0.000826	0.000836
4	597.85	0.0406	0.014	0.011	-0.00433	0.00547
5	597	0.0558	0.0396	0.0176	0.00662	0.00703
6	596.52	0.0646	0.0404	0.0145	0.00151	0.00965
7	594.85	0.0852	0.139	0.0332	-0.0138	0.0162
8	595.42	0.0731	0.0201	0.0258	0.00335	0.0118
9	597.53	0.05	0.016	0.0132	0.00188	0.00429
10	597.21	0.0568	0.00975	0.0167	-0.0136	0.009
11	592.81	0.112	0.139	0.041	0.00975	0.0193
12	549.97	0.33	2.08	0.21	-0.0243	0.0971

Table C.2: Brightness temperatures for 10.7 GHz at 45° incidence.

	I		Q		U	
Profile	T_b	$Error$	T_b	$Error$	T_b	$Error$
1	598.4	0.0285	6.88e-06	4.91e-06	0	0
2	598.19	0.0317	-0.00294	0.00425	-0.00366	0.0026
3	598.27	0.0312	0.00218	0.00466	-0.00306	0.00218
4	597.67	0.0459	-0.0124	0.0117	0.00513	0.0059
5	596.74	0.0596	0.0538	0.0201	0.0121	0.00976
6	596.32	0.0666	0.0282	0.021	-0.0162	0.00912
7	594.39	0.088	0.114	0.0349	-0.00668	0.0174
8	594.93	0.0782	0.044	0.0211	-0.00977	0.0111
9	597.33	0.0535	0.00516	0.0124	-0.000567	0.00793
10	596.89	0.0601	0.0101	0.02	0.0116	0.0109
11	592.4	0.115	0.15	0.0421	0.0124	0.0201
12	549.24	0.33	2.57	0.211	0.0998	0.0928

Table C.3: Brightness temperatures for 10.7 GHz at 50° incidence.

	I		Q		U	
Profile	T_b	$Error$	T_b	$Error$	T_b	$Error$
1	598.28	0.0303	2.19e-05	1.35e-05	-1.12e-05	1.12e-05
2	598.06	0.0336	0.00169	0.00183	-0.000578	0.000859
3	598.14	0.0329	-0.00782	0.00819	-0.00145	0.00251
4	597.51	0.0471	0.0106	0.0101	0.00865	0.00645
5	596.47	0.0634	0.0627	0.0189	-0.0167	0.0093
6	595.94	0.0712	0.066	0.0209	-0.000178	0.00939
7	593.81	0.0974	0.186	0.0357	0.00107	0.0164
8	594.56	0.0815	0.0695	0.0224	0.000961	0.0102
9	597.21	0.0548	0.00983	0.016	0.0017	0.00873
10	596.82	0.061	0.0784	0.0187	0.000938	0.00864
11	591.79	0.12	0.298	0.0413	-0.0186	0.0199
12	547.89	0.333	2.79	0.22	-0.0791	0.091

Table C.4: Brightness temperatures for 10.7 GHz at 55° incidence.

	I		Q		U	
Profile	T_b	$Error$	T_b	$Error$	T_b	$Error$
1	598.1	0.0326	1.76e-05	7.23e-06	0	0
2	597.95	0.0344	0.00257	0.000695	-0.00233	0.00178
3	597.96	0.0363	0.00361	0.00278	0.00194	0.002
4	597.37	0.0463	0.013	0.00985	-0.000593	0.00338
5	596.31	0.063	0.0679	0.0212	0.00671	0.00985
6	595.35	0.0793	0.085	0.0251	-0.015	0.0117
7	593.3	0.1	0.338	0.0364	-0.0372	0.0164
8	593.99	0.0862	0.124	0.027	0.00933	0.0113
9	596.87	0.0612	0.018	0.0152	-0.00222	0.0076
10	596.38	0.0669	0.0264	0.02	-0.00238	0.0102
11	590.95	0.125	0.436	0.0443	0.0101	0.0204
12	546.95	0.335	3.24	0.22	0.173	0.0866

Table C.5: Brightness temperatures for 10.7 GHz at 60° incidence.

	I		Q		U	
Profile	T_b	$Error$	T_b	$Error$	T_b	$Error$
1	597.94	0.0348	1.8e-05	8.77e-06	0	0
2	597.67	0.0374	0.000892	0.00385	0.00116	0.00154
3	597.77	0.0379	0.00263	0.00445	-0.00433	0.00378
4	597.02	0.0511	0.0195	0.00896	-0.0021	0.00448
5	595.82	0.0664	0.131	0.0223	0.00459	0.0104
6	595.08	0.0777	0.103	0.0266	0.000262	0.0101
7	592.55	0.105	0.376	0.0421	-0.0324	0.0185
8	593.48	0.0868	0.0916	0.0303	-0.00226	0.013
9	596.57	0.0611	0.0295	0.0189	-0.000447	0.00884
10	596.04	0.0696	0.0615	0.0198	-0.00986	0.0118
11	589.52	0.136	0.352	0.0471	0.00127	0.0197
12	545.36	0.341	3.29	0.223	0.0279	0.0818

Table C.6: Brightness temperatures for 18.7 GHz at 40° incidence.

	I		Q		U	
Profile	T_b	$Error$	T_b	$Error$	T_b	$Error$
1	594.67	0.0552	-0.000271	0.000308	-0.000223	0.000211
2	594.11	0.06	-0.00327	0.0118	-0.000377	0.00479
3	594.08	0.0625	0.0155	0.011	-0.00859	0.00401
4	592.1	0.0905	0.015	0.0247	0.00413	0.0123
5	588.72	0.125	0.173	0.0518	-0.0302	0.0252
6	586.43	0.147	0.225	0.0573	-0.0378	0.0294
7	579.46	0.198	0.536	0.0932	0.0466	0.0461
8	583.09	0.157	0.254	0.0651	-0.0182	0.0313
9	590.35	0.119	0.0871	0.0425	-0.0213	0.0206
10	588.97	0.132	-0.0104	0.0551	-0.0177	0.025
11	573.38	0.234	0.532	0.108	0.0222	0.0527
12	532.65	0.429	2.08	0.281	-0.0157	0.135

Table C.7: Brightness temperatures for 18.7 GHz at 45° incidence.

	I		Q		U	
Profile	T_b	$Error$	T_b	$Error$	T_b	$Error$
1	594.35	0.0577	3.99e-05	6.03e-06	0	0
2	593.59	0.0636	0.0184	0.00758	-0.00341	0.00526
3	593.73	0.0647	-0.0107	0.0123	0.00582	0.00391
4	591.78	0.0934	0.0541	0.0275	-0.0156	0.0135
5	587.78	0.132	0.258	0.0486	0.0177	0.0245
6	585.76	0.148	0.286	0.0593	-0.0354	0.0295
7	578.29	0.203	0.671	0.0954	0.0182	0.0459
8	582.15	0.16	0.249	0.0629	-0.0181	0.0324
9	589.64	0.122	0.0571	0.0428	0.00644	0.0207
10	587.78	0.144	0.132	0.0533	-0.0628	0.0261
11	572.52	0.232	0.578	0.108	-0.0428	0.0528
12	532.29	0.433	1.97	0.277	0.267	0.132

Table C.8: Brightness temperatures for 18.7 GHz at 50° incidence.

	I		Q		U	
Profile	T_b	$Error$	T_b	$Error$	T_b	$Error$
1	593.85	0.06	4.88e-05	7.44e-06	0	0
2	593.13	0.0661	0.0201	0.0111	0.00519	0.00725
3	593.29	0.0668	-0.0215	0.0107	0.00309	0.00563
4	591.17	0.0952	-0.0212	0.0324	0.0168	0.0167
5	586.9	0.137	0.247	0.0562	-0.00988	0.0255
6	584.65	0.154	0.392	0.0641	-0.0211	0.0298
7	576.72	0.208	0.88	0.0964	0.0204	0.0471
8	580.36	0.172	0.476	0.0659	-0.00245	0.0329
9	589.17	0.12	0.144	0.0432	-0.00651	0.0214
10	587.13	0.144	0.126	0.0546	-0.0311	0.0266
11	570.69	0.237	1.02	0.111	-0.00382	0.0542
12	531.13	0.435	2.86	0.277	-0.0317	0.125

Table C.9: Brightness temperatures for 18.7 GHz at 55° incidence.

	I		Q		U	
Profile	T_b	$Error$	T_b	$Error$	T_b	$Error$
1	593.29	0.0634	0.00187	0.00152	0.000522	0.00105
2	592.61	0.0705	0.016	0.00897	0.00426	0.00429
3	592.6	0.0703	0.00542	0.0127	-0.00455	0.00777
4	590.18	0.102	0.077	0.0333	0.00645	0.0164
5	585.4	0.144	0.341	0.055	-0.0387	0.0261
6	583.26	0.158	0.419	0.0628	-0.0576	0.0312
7	574.42	0.219	1.08	0.104	-0.0668	0.049
8	578.62	0.176	0.45	0.069	-0.00554	0.0339
9	587.83	0.13	0.191	0.0483	-0.0214	0.0245
10	585.72	0.154	0.261	0.0582	-0.00109	0.0288
11	568.21	0.245	1.16	0.115	0.0125	0.0553
12	530.09	0.442	2.63	0.267	-0.0332	0.122

Table C.10: Brightness temperatures for 18.7 GHz at 60° incidence.

	I		Q		U	
Profile	T_b	$Error$	T_b	$Error$	T_b	$Error$
1	592.43	0.0671	5.08e-05	2.18e-05	1.81e-05	1.57e-05
2	591.57	0.0744	0.000695	0.0132	-0.00233	0.00471
3	591.83	0.0739	-0.00934	0.012	0.000949	0.00618
4	589.08	0.106	0.103	0.0371	-0.0227	0.0183
5	583.94	0.149	0.4	0.0596	-0.00541	0.0287
6	581.31	0.167	0.426	0.0674	-0.0126	0.0325
7	571.7	0.229	1.27	0.104	-0.0194	0.052
8	576.36	0.184	0.679	0.0737	0.0462	0.0358
9	586.44	0.138	0.197	0.0496	0.0161	0.0257
10	584.26	0.157	0.241	0.0616	-0.0152	0.0313
11	564.9	0.259	1.4	0.12	-0.00943	0.0572
12	529.36	0.451	3.56	0.267	-0.172	0.115

Table C.11: Brightness temperatures for 37.0 GHz at 40° incidence.

	I		Q		U	
Profile	T_b	$Error$	T_b	$Error$	T_b	$Error$
1	588	0.088	-0.00346	0.00452	0.00101	0.00171
2	584.97	0.118	0.129	0.0402	-0.02	0.0196
3	585.76	0.116	-0.0453	0.0353	0.00164	0.0163
4	573.21	0.231	0.372	0.105	-0.0278	0.0514
5	559.03	0.301	1.25	0.169	0.000181	0.0828
6	551.98	0.334	1.3	0.187	-0.16	0.0918
7	534.3	0.398	2.03	0.254	0.143	0.127
8	545.94	0.329	0.911	0.193	0.108	0.0964
9	564.14	0.295	0.846	0.138	-0.0835	0.07
10	557.05	0.327	1.03	0.166	-0.0842	0.0835
11	527.42	0.413	1.35	0.256	0.155	0.126
12	520.97	0.516	1.78	0.286	0.0496	0.14

Table C.12: Brightness temperatures for 37.0 GHz at 45° incidence.

	I		Q		U	
Profile	T_b	$Error$	T_b	$Error$	T_b	$Error$
1	587.17	0.0913	-0.00673	0.0061	0.000244	0.00228
2	583.91	0.125	0.055	0.0422	-0.0143	0.0216
3	584.76	0.121	0.0753	0.0369	-0.0275	0.0177
4	571.9	0.235	0.417	0.109	0.00396	0.0525
5	556.54	0.31	1.27	0.171	0.142	0.0857
6	548.97	0.346	1.74	0.189	0.0705	0.0937
7	532.25	0.399	2.3	0.254	0.0723	0.126
8	543.02	0.335	1.19	0.196	-0.0195	0.097
9	562.03	0.303	0.964	0.146	-0.148	0.072
10	554.27	0.337	1.31	0.172	0.0879	0.0857
11	524.18	0.422	1.64	0.252	-0.0978	0.126
12	519.97	0.521	2.25	0.279	-0.00657	0.138

Table C.13: Brightness temperatures for 37.0 GHz at 50° incidence.

	I		Q		U	
Profile	T_b	$Error$	T_b	$Error$	T_b	$Error$
1	585.97	0.0959	-0.00174	0.0074	-9.94e-05	0.0027
2	582.68	0.13	0.0487	0.0444	-0.00559	0.0219
3	583.64	0.126	0.00612	0.036	0.0154	0.0178
4	569.83	0.243	0.481	0.107	0.0144	0.0537
5	554.25	0.313	1.69	0.176	0.0555	0.0862
6	546.37	0.351	1.7	0.19	0.209	0.0938
7	528.8	0.41	3.22	0.26	0.234	0.128
8	539.46	0.346	1.2	0.2	0.0131	0.0989
9	558.96	0.313	1.05	0.151	0.0415	0.0738
10	550.73	0.351	1.86	0.18	0.0854	0.0883
11	521.46	0.431	1.37	0.261	-0.0137	0.126
12	520.1	0.531	1.96	0.278	0.0516	0.138

Table C.14: Brightness temperatures for 37.0 GHz at 55° incidence.

	I		Q		U	
Profile	T_b	$Error$	T_b	$Error$	T_b	$Error$
1	584.84	0.0993	-0.00433	0.00778	-0.00266	0.00181
2	580.98	0.136	0.0685	0.0457	0.00486	0.021
3	582.05	0.132	0.0346	0.0382	-0.0429	0.0199
4	567.05	0.254	0.483	0.112	0.0279	0.0559
5	551	0.322	1.92	0.178	-0.104	0.0879
6	542.21	0.361	2.12	0.198	0.03	0.096
7	524.91	0.418	2.71	0.262	0.117	0.126
8	536.62	0.35	1.89	0.204	0.0088	0.101
9	555.15	0.328	1.53	0.158	0.0831	0.0779
10	546.33	0.364	2	0.187	-0.0407	0.0918
11	516.61	0.445	1.72	0.261	0.268	0.129
12	518.57	0.535	2.4	0.273	-0.0112	0.13

Table C.15: Brightness temperatures for 37.0 GHz at 60° incidence.

	I		Q		U	
Profile	T_b	$Error$	T_b	$Error$	T_b	$Error$
1	583.13	0.105	-6.19e-05	0.00495	0.000541	0.00243
2	578.61	0.145	0.214	0.0492	-0.0313	0.0246
3	579.92	0.14	0.114	0.0423	-0.0179	0.0204
4	563.58	0.265	0.756	0.123	0.0327	0.0588
5	546.85	0.331	2.09	0.184	0.0486	0.0898
6	537.28	0.376	2.64	0.206	0.000662	0.1
7	520.55	0.429	3.02	0.264	0.0558	0.129
8	531.25	0.362	2.51	0.213	-0.0593	0.104
9	549.9	0.347	1.16	0.163	0.0722	0.0817
10	540.88	0.38	2.22	0.195	0.00841	0.095
11	511.92	0.457	2.45	0.259	0.105	0.127
12	516.99	0.546	3.01	0.262	-0.183	0.127

LIST OF REFERENCES

[1] G. A. Poe, "Review of satellites-historical perspective," Feb 1997.

[2] J. Simpson, R. F. Adler, and G. R. North, "A proposed tropical rainfall measureing mission (TRMM) satellite," *Bulletin of the American Meteorological Society*, vol. 69, no. 3, pp. 278–295, Mar 1988.

[3] C. Kummerow, W. S. Olson, and L. Giglio, "A simplified scheme for obtaining precipitation and vertical hydrometeor profiles from passive microwave sensors," *IEEE Transactions on Geoscience and Remote Sensing*, vol. 34, no. 5, pp. 1213–1232, Sep 1996.

[4] P. W. Gaiser, K. M. St.Germain, E. M. Twarog, G. A. Poe, W. Purdy, D. Richardson, W. Grossman, W. L. Jones, D. Spencer, G. Golba, J. Cleveland, L. Choy, R. M. Bevilacqua, and P. S. Chang, "The WindSat spaceborne polarimetric microwave radiometer: sensor description and early orbit performance," *IEEE Transactions on Geoscience and Remote Sensing*, vol. 42, no. 11, pp. 2347–2361, Nov 2004.

[5] I. S. Adams, C. C. Hennon, W. L. Jones, and K. A. Ahmad, "Evaluation of hurricane ocean vector winds from WindSat," *IEEE Transactions on Geoscience and Remote Sensing*, vol. 44, no. 3, pp. 656–667, Mar 2006.

[6] M. H. Bettenhausen, C. K. Smith, R. M. Bevilacqua, N.-Y. Wang, P. W. Gaiser, and S. Cox, "A nonlinear optimization algorithm for WindSat wind vector retrievals," *IEEE Transactions on Geoscience and Remote Sensing*, vol. 44, no. 3, pp. 597–609, Mar 2006.

[7] K. N. Liou, *An Introduction to Atmospheric Radiation.* San Diego: Academic Press, 2002.

[8] J. D. Jackson, *Classical Electrodynamics.* New York: John Wiley and Sons, 1998.

[9] M. I. Mishchenko, L. D. Travis, and A. A. Lacis, *Scattering, Absorption, and Emission of Light by Small Particles.* New York: NASA Goddard Institute for Space Sciences, 2005.

[10] C. F. Bohren and D. R. Huffman, *Absorption and Scattering of Light by Small Particles.* Weinheim: Wiley VCH Verlag GmgH and Co. KGaA, 2004.

[11] C. A. Balanis, *Advanced Engineering Electromagnetics*. New York: John Wiley and Sons, 1989.

[12] L. Tsang, J. A. Kong, and R. T. Shin, *Theory of Microwave Remote Sensing*. New York: Jonh Wiley and Sons, 1985.

[13] S. Chandrasekhar, *Radiative Transfer*. New York: Dover Publications, Inc., 1960.

[14] P. C. Waterman, "Matrix formulation of electromagnetic scattering," *Proc. IEEE*, vol. 53, no. 8, pp. 805–812, Aug 1965.

[15] ——, "Symmetry, unitarity, and geometry in electromagnetic scattering," *Phys. Rev. D*, vol. 3, no. 4, pp. 825–839, Feb 1971.

[16] W.-K. Tao and J. Simpson, "The Goddard Cumulus Ensemble model. part I: Model description," *Terrestrial, Atmospheric, and Oceanic Sciences*, vol. 4, no. 1, pp. 35–72, Mar 1993.

[17] J. Simpson and W.-K. Tao, "The Goddard Cumulus Ensemble model. part II: Applications for studying cloud precipitating process and for NASA TRMM," *Terrestrial, Atmospheric, and Oceanic Sciences*, vol. 4, no. 1, pp. 73–116, Mar 1993.

[18] P. J. Webster and R. Lukas, "TOGA COARE: The coupled ocean–atmosphere response experiment," *Bulletin of the American Meteorological Society*, vol. 73, no. 9, pp. 1377–1416, Sep 1992.

[19] J. S. Marshall and W. M. Palmer, "The distribution of raindrops with size," *Journal of Meteorology*, vol. 5, pp. 165–166, Aug 1948.

[20] K. N. Liou, *Radiation and Cloud Processes in the Atmosphere*. New York: Oxford University Press, 1992.

[21] C. Davis, *PyArts User Guide*, 2006.

[22] G. M. McFarquhar and A. J. Heymsfield, "Parameterization of tropical cirrus ice crystal size distributions and implications for radiative transfer: results from cepex," *Journal of the Atmospheric Sciences*, vol. 54, no. 17, pp. 2187–2200, Sep 1997.

[23] T. Oguchi, "Electromagenetic wave propagation and scattering in rain and other hydrometeors," *Proceedings of the IEEE*, vol. 71, no. 9, pp. 1029–1079, Sep 1983.

[24] K. Andsager, K. V. Beard, and N. F. Laird, "Laboratory measurecments of axis ratios for large raindrops," *Journal of the Atmospheric Sciences*, vol. 56, no. 15, pp. 2673–2683, Aug 1999.

[25] H. J. Liebe, T. Manabe, and G. A. Hufford, "Millimeter-wave attenuation and delay rates due to fog/cloud conditions," *IEEE Transactions on Antennas and Propagation*, vol. 37, no. 12, pp. 1617–1623, Dec 1989.

[26] J. C. Maxwell Garnett, "Colours in metal glasses and metallic films," *Royal Society of London Philosophical Transactions Series A*, vol. 203, pp. 385–420, 1904.

[27] S. A. Buehler, P. Eriksson, T. Kuhn, A. von Engeln, and C. Verdes, "ARTS, the atmospheric radiative transfer simulator," *Journal of Quantitative Spectroscopy and Radiative Transfer*, vol. 91, no. 1, pp. 65–93, Jan 2005.

[28] H. Liebe and D. Layton, "Millimeter-wave properties of the atmosphere: Laboratory studies and propagation modelling," US. Dept. of Commerce, National Telecommunications and Information Administration, Institute for Communication Sciences, Tech. Rep., 1987.

[29] H. J. Liebe, "MPM – an atmospheric millimeter-wave propagation model," *International Journal of Infrared and Millimeter Waves*, vol. 10, no. 6, pp. 631–650, Jun 1989.

[30] H. J. Liebe, G. A. Hufford, and M. G. Cotton, "Propagation modeling of moist air and suspended water/ice paritcles at frequencies below 1000 ghz," in *AGARD 52nd Specialist Metting of the Electromagnetic Wave Propagation Panel*, Palma de Mallorca, Spain, 1993.

[31] P. W. Rosenkranz, "Water vapor microwave conitnuum absorption: A comparison of measurements and models," *Radio Science*, vol. 33, no. 4, pp. 919–928, Apr 1998.

[32] ——, "Correction to 'water vapor microwave conitnuum absorption: A comparison of measurements and models'," *Radio Science*, vol. 34, no. 4, p. 1025, Apr 1999.

[33] S. Buehler, P. Eriksson, W. Haas, N. Koulev, T. Kuhn, and O. Lemke, *ARTS User Guide, ARTS version 1.0.173*, Mar 2005. [Online]. Available: http://www.sat.uni-bremen.de/arts/docs.php

[34] P. J. Flatau, R. L. Walco, and W. R. Cotton, "Polynomial fits to saturation vapor pressure," *Journal of Applied Meteorology*, vol. 31, no. 12, pp. 1507–1510, Dec 1992.

[35] P. Eriksson and S. Buehler, *ARTS User Guide, ARTS Version 1.1.1095*, Mar 2006. [Online]. Available: http://www.sat.uni-bremen.de/arts/docs.php

[36] C. Davis, C. Emde, and R. Harwood, "A 3D polarized reverse monte carlo radiative transfer model for mm and sub-mm passive remote sensing in cloudy atmospheres," *IEEE Transactions on Geoscience and Remote Sensing*, vol. 43, no. 5, pp. 1096–1101, May 2005.

[37] M. I. Mishchenko, "Calculation of the amplitude matrix for a nonspherical particle in a fixed orientation," *Applied Optics*, vol. 39, no. 6, Feb 2000.

[38] M. I. Mishchenko and L. D. Travis, "Capabilities and limitations of a current fortran implimentation of the t-matrix method ofr randomly oriented, rotationally symmetric scatterers," *Journal of Quantitative Spectroscopy and Radiative Transfer*, vol. 60, no. 3, pp. 309–324, Sep 1998.

[39] K. Aydin, "Centimeter and millimeter wave scattering from nonspherical hydrometeors," in *Light Scattering by Nonspherical Particles*, M. I. Mishchenko, J. I. Hovenier, and L. D. Travis, Eds. San Diego: Academic Press, 2000, pp. 451–479.

[40] J. L. Haferman, "Microwave wave scattering by precipitation," in *Light Scattering by Nonspherical Particles*, M. I. Mishchenko, J. I. Hovenier, and L. D. Travis, Eds. San Diego: Academic Press, 2000, pp. 481–424.

[41] L. Roberti and C. Kummerow, "Monte carlo calculations of polarized microwave radiation emerging from cloud structures," *Journal of Geophysical Research*, vol. 104, no. D2, pp. 2093–2104, Jan 1999.

[42] B. Kutuza, G. Zagorin, A. Hornbostel, and A. Schroth, "Physical modeling of passive polarimetric microwave observations of the atmosphere with respect to the third stokes parameter," *Radio Science*, vol. 33, no. 3, pp. 677–695, Jun 1998.